UNIVERSITY OF CALIFORNIA, SAN DIEGO

New Nano Structure Approaches for Bulk Thermoelectric Materials

A dissertation submitted in partial satisfaction of the

requirements for the degree Doctor of Philosophy

in

Materials Science and Engineering

by

Jeonghoon Kim

Committee in Charge:

Professor Sungho Jin, Chair
Professor Ami Berkowitz, Co-Chair
Professor Prabhakar Bandaru
Professor Renkun Chen
Professor Yu Qiao

2010

The dissertation of Jeonghoon Kim is approved, and it is acceptable in quality and form for publication on microfilm and electronically:

_____

_____

_____

_____
Co-Chair

_____
Chair

University of California, San Diego

2010

Dedicated to

Misun, Sungchan, Sungbin, Habin

and

my parents

"Christ Himself, in whom are hidden all the treasures of wisdom and knowledge."

Col 2:3

TABLE OF CONTENTS

LIST OF FIGURES

LIST OF TABLES

ACKNOWLEDGEMENTS

I would like to express my deep gratitude to my advisor, Professor Sungho Jin for his strong encouragement, support, and guidance throughout my Ph.D. study. I wish to express my gratefulness to my committee members for their time and helpful suggestions: Professor Ami Berkowitz, Professor Prabhakar Bandaru, Professor Yu Qiao, and Professor Renkun Chen. Especially, Professor Ami Berkowitz inspired me about research and Professor Renkun Chen gave great help for measurement techniques.

I would also like to recognize and thank the following individuals for their assistance in various aspects of this work: Professor Kenneth Vecchio, Dr. Fred Spada, Dr. Leon Chen, Jae-Yun Moon, Phi Nguyen, Chulmin Choi, Young Oh, Hyunsoo Kim, Kunbae Noh, Seong Deuk Kong, and Hyunwoo Noh. I appreciate all the help from my collaborators. We have shared joy and frustration together solving countless materials, fabrications, and device problems in the past years.

I deeply appreciate Charlotte Lauve, Betty Manoulian, Iris Villanueva, and Aimee Sung for taking care of the administrative burdens for me.

Most of all, I am so grateful to my wife Misun, my sons Sungchan and Paul, my daughter Claire, and our parents in Korea for their love and prayer.

Finally, I would like to acknowledge the support of Samsung Fellowship during my research period.

VITA

1971	Born in Seoul, South Korea
1999	B.S., Mechanical Engineering, Penn State University, University Park, Pennsylvania
2001	M.S., Mechanical Engineering, Virginia Tech, Blacksburg, Virginia
2005	Samsung SDI institute of technology Suwon, South Korea
2010	Ph.D., Materials Science and Engineering, University of California, San Diego

ABSTRACT OF THE DISSERTATION

New Nano Structure Approaches for Bulk Thermoelectric Materials

by

Jeonghoon Kim

Doctor of Philosophy in Materials Science and Engineering

University of California, San Diego, 2010

Professor Sungho Jin, Chair

Professor Ami Berkowitz, Co-Chair

A sustainable supply of environmentally clean energy is one of the most significant challenges facing the 21st century as fossil fuel supplies are decreasing and world energy demand keeps increasing. The field of thermoelectric (TE) materials and devices, for efficient solid state cooling and power generation, has expanded significantly in recent years partly due to the advent of nanotechnology and the promise of higher efficiencies of electrical energy versus thermal energy inter-conversion[1,2]. Such solid-state refrigeration and power generation based on thermoelectric phenomenon offer significant promises to technical applications in the computer, energy conversion, and consumer market applications. While the area itself has been investigated since the 1950's, traditional bulk thermoelectric materials, such as Bi_2Te_3 generally had low

efficiencies (~ 6 %) for commercial energy conversion applications. However, a deeper utilization of nanoscience at the quantum mechanical level and fabrication of lower dimensional materials such as nanowires and quantum wells, has shown promise of greatly increasing the energy conversion efficiency [3]. Lower dimensional materials, such as nanoscale thin films and nanowires, have been predicted to have large thermoelectric figures of merit and conversion efficiencies of waste heat to useful energy for practical application, and there are strong indications that this is possible [4]. However, ultimately one needs large volumes of active thermoelectric material for an overall high efficiency. This is, at the present time, not feasible as the typical manufacturing of bulk volumes from low dimensional structures is time consuming and difficult. In this thesis, we lay out several practical schemes to incorporate nanoscale features in bulk-fabricated thermoelectric materials for easy fabrication and a high thermoelectric figure of merit, ZT. We propose to fabricate a novel nanostructure material to impart low dimensional confinement and nanoscale defects for a high figure of merit. Various unique architectures and associated process techniques as well as device applications are introduced. It is anticipated that these techniques will lead to many novel thermoelectric materials, innovative and useful materials processing technologies, and technical applications for efficient thermal management and energy conversion of sunlight and automobile waste heat.

CHAPTER 1: Introduction

1.1 Introduction to Thermoelectrics

1.1.1 Background

As fossil energy resources are running out and their environmental concerns are increasing, clean and sustainable energy resources and related technologies are receiving more and more spot lighting. It is also a great issue to minimize the amount of wasted energy from low energy conversion efficiencies. Among the leading technologies to overcome the situations, thermoelectric materials are gaining new attention because of their potential to solve the issues mentioned above. Thermoelectric materials can directly convert wasted heat energy into electricity; environmentally friendly refrigeration can be achieved without harmful exhaust gases [1]. Thermoelectric materials are solid state devices meaning they have no moving parts, which offers the merits of no noise, geometrical freedom, and high reliability. Despite these merits, thermoelectric materials have not been used extensively for many years due to low efficiencies compared to mechanical energy conversion systems. Its application has been limited to a few niche markets where extremely high reliability or simplicity is required such as space mission projects. However, recent thermoelectric studies have shown remarkable improvement in the energy conversion efficiency through innovated nanostructures [2, 3]. With these developing nanotechnologies, thermoelectric materials are becoming more and more suitable for many areas including energy harvesting, clean energy refrigeration, temperature control on electronics, and so on.

1.1.2 Applications

The reason thermoelectric materials are receiving so much renewed attention is due to their extensive applications. First of all, a thermoelectric device can serve as a power generator using wasted heat energy. According to US Department of Energy office (Figure 1), about 60% of total energy (more than 1.72 billion barrels of oil) is wasted every year during energy conversion processes. If TE devices can revive 10% of wasted energy, their value could be equivalent to several billions of dollars per year. Many energy and automobile companies are carrying research to extract energy from these wasted heat streams and to enhance its efficiency. Also, it will result in less pollution of air such as CO2 emissions from fossil energy resources.

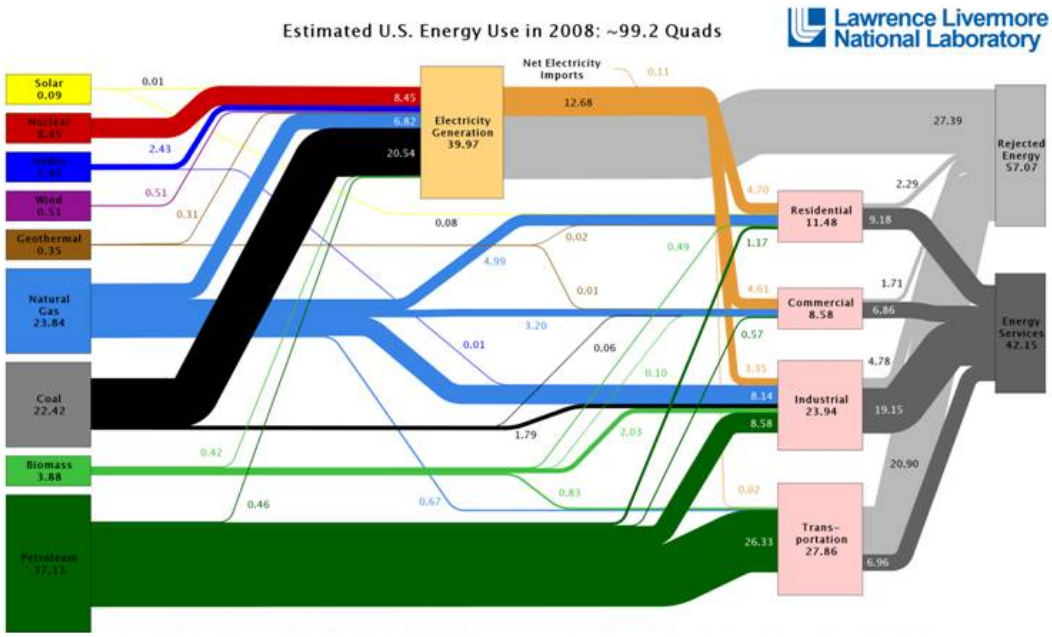

Figure 1. U.S. Energy use in 2008: 100 quadrillion BTU of primary energy and 60 quadrillion of wasted energy. Advanced waste heat recovery technology can improve overall efficiency and reduce fuel consumption in automobiles and power plants.

Besides wasted thermal energy recovery, many research groups are working on solar thermal energy to generate electric power by using solar energy [2]. Thermoelectric devices can also serve as a solid state refrigerator, which includes various cooling applications such as air-conditioners and water cooler. It will also reduce harmful coolant gases such as chlorofluorocarbons (CFCs) during refrigeration [2]. Figure 2 shows some examples of applications including a car (BMW) with a thermoelectric generator and radiator, bio-medicine applications using the temperature difference between the human body and the ambient air, electronic cooling for CPUs, and so on. Due to its simplicity and reliability, a large potential market for thermoelectric devices beyond the applications described above is coming around the corner.

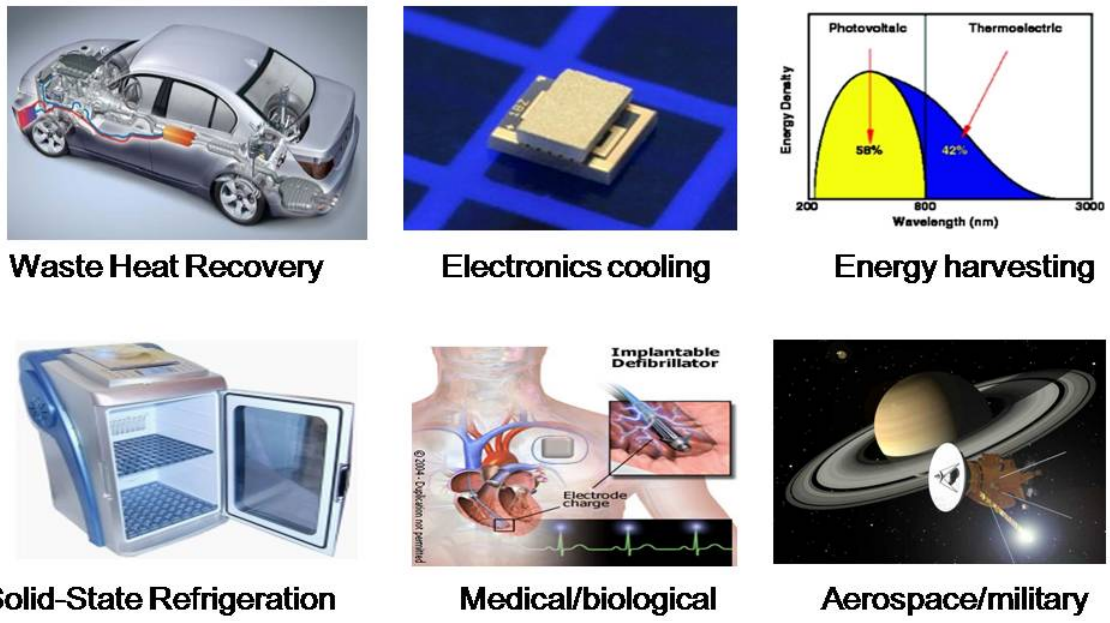

Figure 2. Thermoelectric applications; shows a BMW car with a thermoelectric generator and radiator, electronic cooling for CPUs, solar thermal energy harvesting, solid-state refrigerator, bio-medicine applications using the human body temperature and aerospace applications.

1.2 Thermoelectrics principles

1.2.1 The Seebeck Effect

In 1821 Thomas Johann Seebeck discovered the thermoelectric effect. He found a magnetic compass needle is deflected by a circuit made of two different materials that have a temperature difference between the junctions. At first, he thought a magnetic field is created by the temperature difference, but it was later proved that an electric current is created by a temperature gradient. The electric current consequently generated a magnetic field. This phenomenon is called the Seebeck effect after his name and is termed thermoelectricity. A voltage difference is generated due to the inhomogeneous charge distribution by the temperature difference. This voltage difference generated by a temperature gradient between two junctions is called the Seebeck voltage, and its proportional constant is the Seebeck coefficient defined as the ratio of the voltage produced per the unit temperature gradient.

$$S = \frac{V}{Th - Tc}$$

V is the voltage potential and T_h and T_c are the temperatures of two junctions. The sign of the Seebeck coefficient depends on the direction of voltage potential. When a thermoelectric material shows a positive Seebeck coefficient, we define this as a p-type thermoelectric material in which electricity is carried by positive charges. Inversely, when a thermoelectric material shows a negative Seebeck coefficient, we define this as an n-type thermoelectric material in which electricity is carried by negative charges. Figure 3 shows a Seebeck effect diagram - a thermoelectric device creates a voltage when there is a different temperature on each side. An applied temperature gradient causes charge

carriers in the material, whether they are electrons or electron holes, to diffuse from the hot side to the cold side.

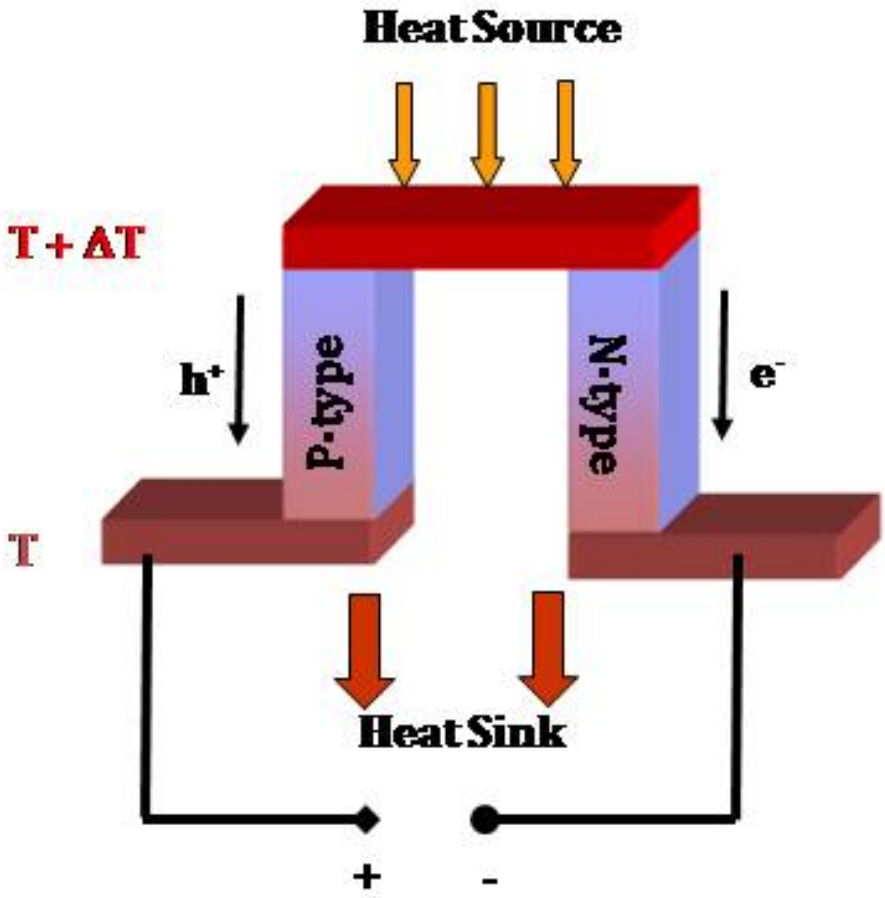

Figure 2. Seebeck effect diagram; A thermoelectric device creates a voltage when there is a different temperature on each side. An applied temperature gradient causes charged carriers in the material, whether they are electrons or electron holes, to diffuse from the hot side to the cold side.

1.2.2 The Peltier Effect

After the Seebeck effect was discovered, French scientist Jean Charles Athanase Peltier discovered an opposite effect: when a current is injected into a circuit that has interfaces of two different materials, heat can be rejected or absorbed at the interfaces. When the direction of current changes, the heat rejection and absorption site is also changed. This phenomenon is called the Peltier effect and can be expressed by the formula:

$$Q = \Pi I$$

where Q is the heat, Π is the Peltier coefficient, and I is the current. The Peltier coefficient is a parameter that represents how much thermal energy can be carried per charge carrier. The materials with a positive Peltier coefficient is p-type and reversely, materials with a negative Peltier coefficient is n-type. Figure 4 shows a Peltier effect diagram - when a current I is made to flow through the circuit, heat is evolved at the upper junction and absorbed at the lower junction. The Peltier effect enables thermoelectric devices to work as a solid state refrigerator or a heater depending on the direction of the current. Theoretically, the amount of absorbed heat at one end and rejected heat at the other end should be the product of the Peltier coefficient and driving current, but the Peltier effect loses efficiency due to Joule heating and conducted heat. The Joule heating becomes dominant as the driven current increases and reaches maximum current where no more cooling happens due to the Joule and conducted heating.

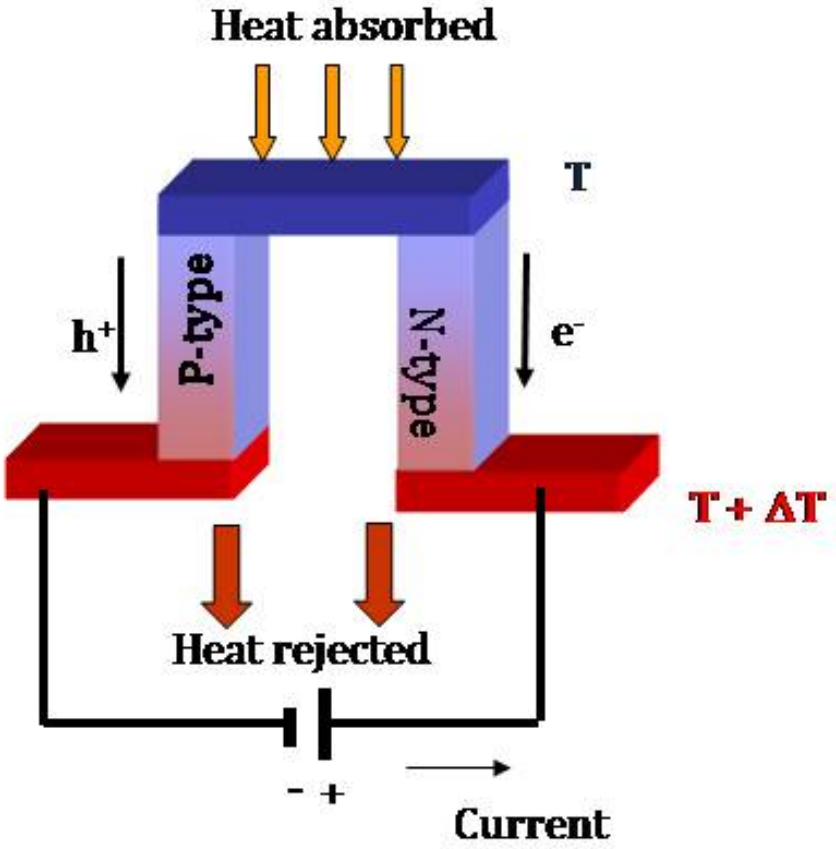

Figure 4. Peltier effect diagram: When a current *I* is made to flow through the circuit, heat is evolved at the upper junction, and absorbed at the lower junction.

1.2.3 The Thomson Effect

In 1851, William Thomson (Lord Kelvin) predicted and discovered experimentally that heating or cooling takes places in a current-carrying conductor that has a temperature gradient. Thomson also found the relationship between the Seebeck and Peltier coefficients, which can be expressed in formula:

$$\Pi = ST$$

where Π is the Peltier coefficient, S is the Seebeck coefficient and T is the absolute temperature. The amount of voltage can be maximized when p-type and n-type thermoelectric materials are connected because their Seebeck coefficients have opposite signs.

1.3 Material properties and measurement in thermoelectrics

The efficiency of thermoelectric devices is expressed by the dimensionless figure of merit, $ZT = S^2\sigma T/K$, where S is Seebeck coeffient, σ is electrical conductivity, K is thermal conductivity and T is the absolute temperature. The characteristics of each property and measurement techniques will be discussed in this section.

1.3.1 Electrical conductivity and Seebeck coefficient

In thermoelectricity, electrical conductivity should be high enough to increase the figure of merit. Electrical conductivity is calculated by measuring electrical resistivity of the materials. Electrical resistivity can be found using the slope of the Voltage versus Current (*V-I*) curves found by measuring a voltage drop while passing a known current through a thermoelectric sample. The voltage measurements are performed usually in

both a forward current direction and a reverse current direction to minimize the contact resistance and Seebeck voltages. It is also recommended to use an AC current to decrease the temperature difference, caused by Peltier effect, which will generate a Seebeck voltage between two probes [1]. There are two major methods to measure the electrical resistivity: the two-probe method and the four-probe method. The two-probe method is simple but easy to have systematic errors because this method requires uniform current through the sample; it is not easy to perfectly remove the contact resistances between the sample and electrode. The four-probe method is more popular because of the systematic disadvantages of the two-probe method. In the four-probe method, two voltage probes are located between two outside current probes. The four-probe method assumes that current flows in one dimension [2]. Because the four-probe method does not take into account the potential in the direction of the thickness, it is more appropriate for thin film samples. However, it is shown that a few millimeter thickness samples can be measured with reasonable accuracy.

The Seebeck coefficient does not depend on the geometry of the sample and is not sensitive to the heat loss. However, the Seebeck coefficient measurement assumes that the material is homogeneous and isotropic [2]. The Seebeck coefficient measurement is measuring the temperature and voltage generated at the end junctions. The slope of the voltage gradient versus the temperature gradient is called the Seebeck coefficient; $S=-\Delta V/\Delta T$. The voltage can fluctuate unless a good electrical contact is made. The temperature gradient is usually induced by heaters. These days, a thermoelectric heater is also a good method of choice to control the temperature precisely. For accurate

measurements, the Seebeck voltage induced by the thermocouples should be compensated.

In this research, electrical conductivity σ and Seebeck coefficient S of the block-shaped TE samples are measured by a custom-made setup as shown in Fig. 5, which is currently being used by professor Renkun Chen's group.

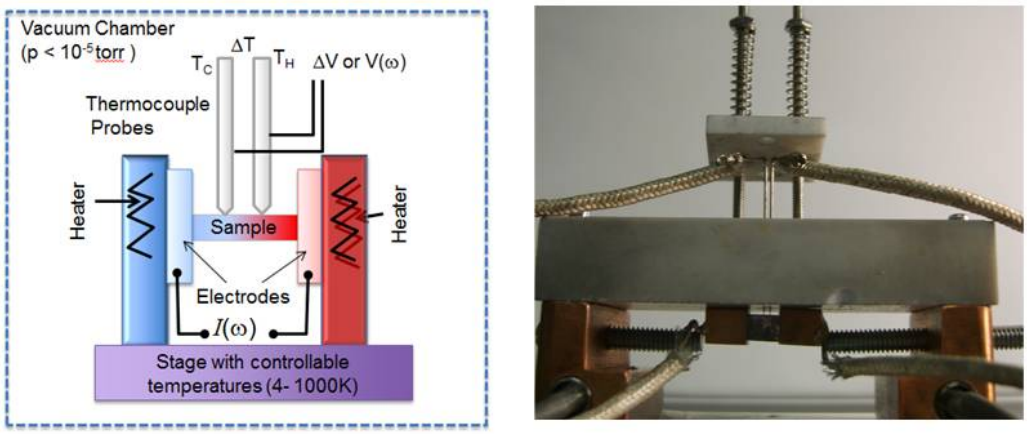

Figure 5: (Left) Schematics and (Right) Photograph of the TE measurement setup used in the Professor Renkun Chen's laboratory.

The sample is sandwiched by two Cu electrodes with solder. Two thermocouple probes spaced 1-3 mm apart, are spring loaded onto the top surface of the sample. The R measurement mechanism is based on the standard four-point probe method where R (= dV/dI) is measured by passing AC current $I(\omega)$ through the two electrodes and measuring $V(\omega)$ from the inner probes. The limits of the resistance measurement is that the current

must be small such that the Joule heating term can be neglected and that the modulation frequency ω be high such that the Peltier heat alternates signs and cancels due to periodic heating and cooling at the junctions (note that a *constant* temperature gradient that might be present throughout the sample will not affect the measurement since *R* is determined by the *slope* of V(ω) *vs* I(ω)). Seebeck coefficient *S* is also measured by the same fixture. Seebeck coefficient *S* is determined by $S = \Delta V / \Delta T$ - thermoelectric voltage (ΔV) developed in response to a temperature difference (ΔT). Heaters attached to either side of the electrode is powered up to create ΔT. ΔV and ΔT is simultaneously measured by the thermocouple probes. In the actual measurement, *S* is determined from the slope of ΔV *vs* ΔT.

1.3.2 Thermal conductivity

The determination of the thermal conductivity is of great interest because it contributes to the performance of thermoelectric materials. Thus, many research groups are working on increasing the efficiency of the thermoelectric materials by reducing the thermal conductivity.

In the case of thin films or superlattices, the transport properties can differ considerably from equivalent bulk materials and also vary depending on sample preparation. It should be pointed out that the in-plane and cross-plane thermal conductivity (heat flow perpendicular to the film) can also differ substantially because of anisotropic film structure (i.e. polycrystalline columnar films, anisotrope materials or superlattices).

Thermal conductivity measurement is generally difficult on two dimensional structures as well as three dimensional geometries, especially on random shapes and sizes. The traditional method to measure the thermal conductivity is the steady state method, which measures the temperature change by heat flux calculated from electrical power consumption; $k=-q''/\nabla T$ [2]. However, it is very difficult to measure exact thermal conductivity. Problems arise because of the thermal radiation, the heat loss in the temperature measuring probes, and the difficulties in measuring the power supplied to the sample with high accuracy. Therefore, methods that can minimize the errors are widely studied in thermoelectric research. One of these is the laser flash technique that uses a light pulse to measure the diffusion time of the temperature in the direction of thickness [2]. A measurement should be done within a short time to minimize the heat loss. Another method is 3ω-method [2]. In this paper, the thermal conductivity κ of the bulk Bi-Sb-Te TE samples is measured by the standard 3ω method (Figure 6a-c). The method employs a metallic strip in intimate contact with the specimen surface. An ac electrical current modulated at angular frequency ω is induced to flow in the strip causing heat generation in the strip. The heating has both a dc component which changes the average temperature of the specimen and an ac component at 2ω which generates thermal waves in the specimen. Because the electrical resistance of the strip depends on the temperature, the resistance will be modulated at 2ω as well. Therefore, there will be an ac voltage drop across the ends of the strip at 3ω, $V_{3\omega}$ (Figure 6a), which is proportional to the ac temperature variation of the strip at 2ω, $T_{2\omega}$. T_2 will depend on the thermal conductivity, *k*, of each underlying material. Thus, one can extract *k* from a measurement of $V_{3\omega}$ vs ω

by the following equation[1]: $\Delta T_{surf}(\omega) = \frac{P}{2\pi kL} \ln 2\omega$, where ΔT_{surf} is the measured temperature change on the sample surface; P is the applied heating power, L is the length of the heater strip. As shown in the equation, $V_{3\omega}$ is proportional to $\ln \omega$, which is also what is observed experimentally (Figure 6c) to extract k.

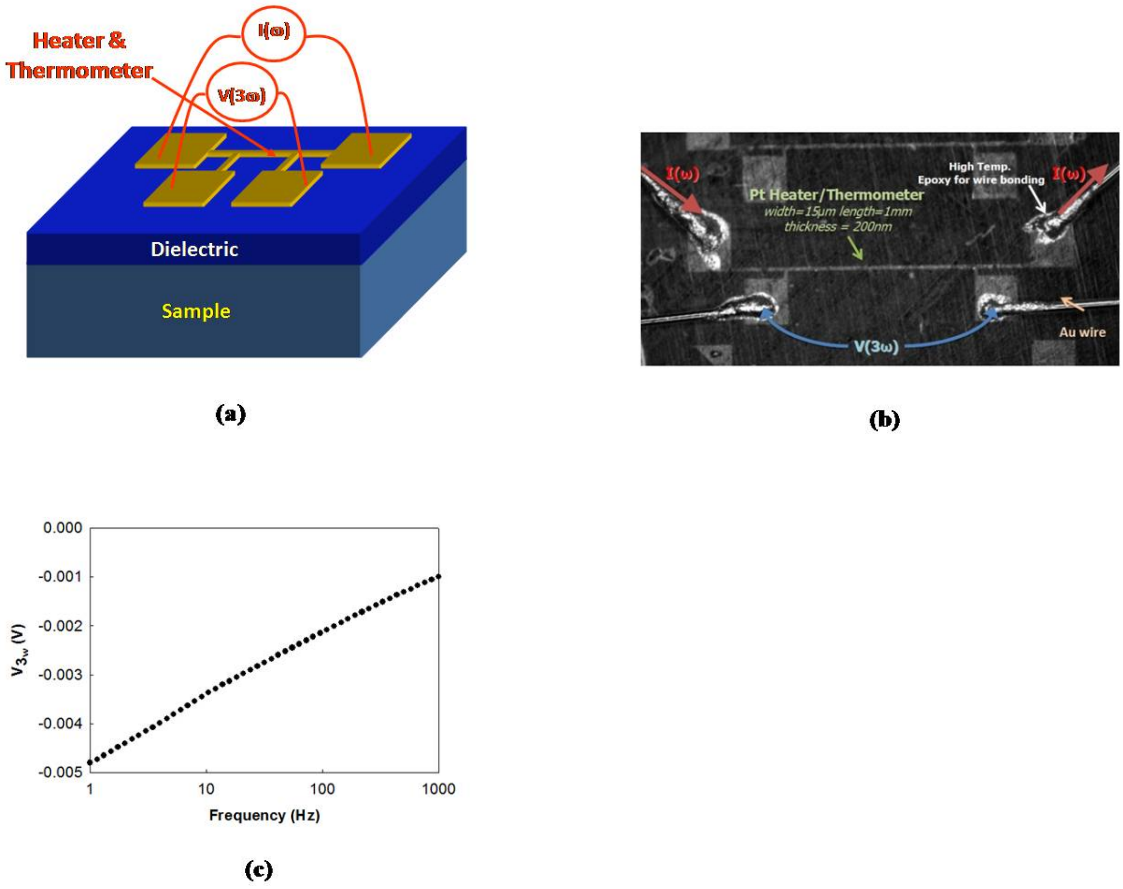

Figure 6. 3ω measurement: (a) schematic of the measurement device; (b) micrograph of a heater deposited SiO2 surface on a Bi-Sb-Te sample. (c) $V_{3\omega}$ vs. frequency (log scale) plot.

Since our Bi-Sb-Te samples are conducting, a layer of dielectric material is deposited on top of the sample to insulate the metal strip from the substrate (Figure 6a). Several dielectric materials and deposition processes have been tried for this application with each process optimized for samples with various surface morphologies and sintering parameters, namely, SiO_2 deposited by plasma enhanced chemical vapor deposition (PECVD, at 350^{o}C) or sputtering (near room temp), Al_2O_3 deposited by atomic layer deposition (ALD at 150^{o}C), or parylene by vapor deposition (at 100^{o}C). Figure 6b shows a sample with PECVD SiO_2 layer and metal strip made of Au. First, the method has been calibrated on a standard Pyrex sample (Pyrex 1770, with k = 1.15 at 300K).

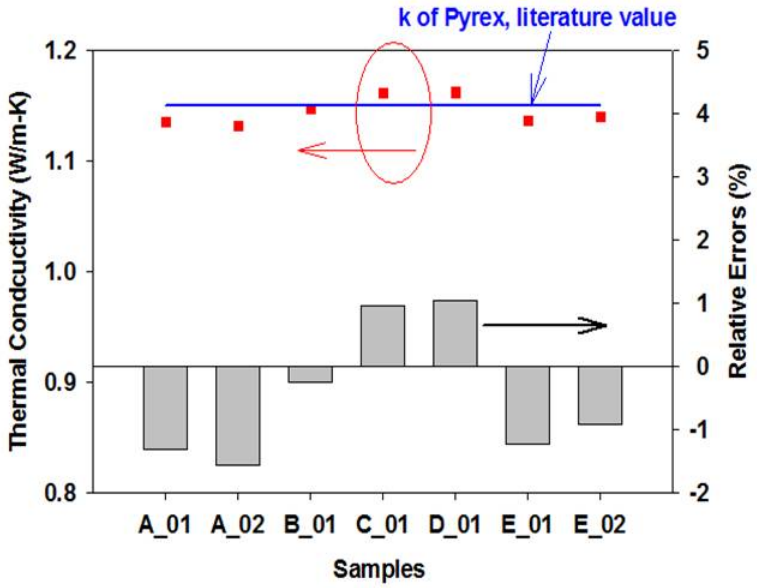

Figure 7. Measured k of Pyrex 1770 matches with literature value (1.15 W/m-K at 300 K).

As shown in Figure 7, our measured *k* values of the Pyrex samples from multiple 3ω measurements match excellently with literature data, with relative errors not larger than 2%. This shows the high accuracy and repeatability of our 3ω measurement technique. Using this method, we have successfully measured a variety of the TE samples prepared from different processes. The 3ω method can also be used to measure *k* of thin film TE samples. As shown in Figure 8a-b, measurements on both thin film sample and reference sample (without the film) can be used to calculate the temperature difference ΔT across the thin film. As shown in Figure 8c, ΔT is a constant and is independent of the frequency for the given frequency range. Thermal conductivity *k* of the film can then be calculated from $k = q''d / \Delta T$, where q'' is the applied heat flux of the heater strip and *d* is the thickness of the film.

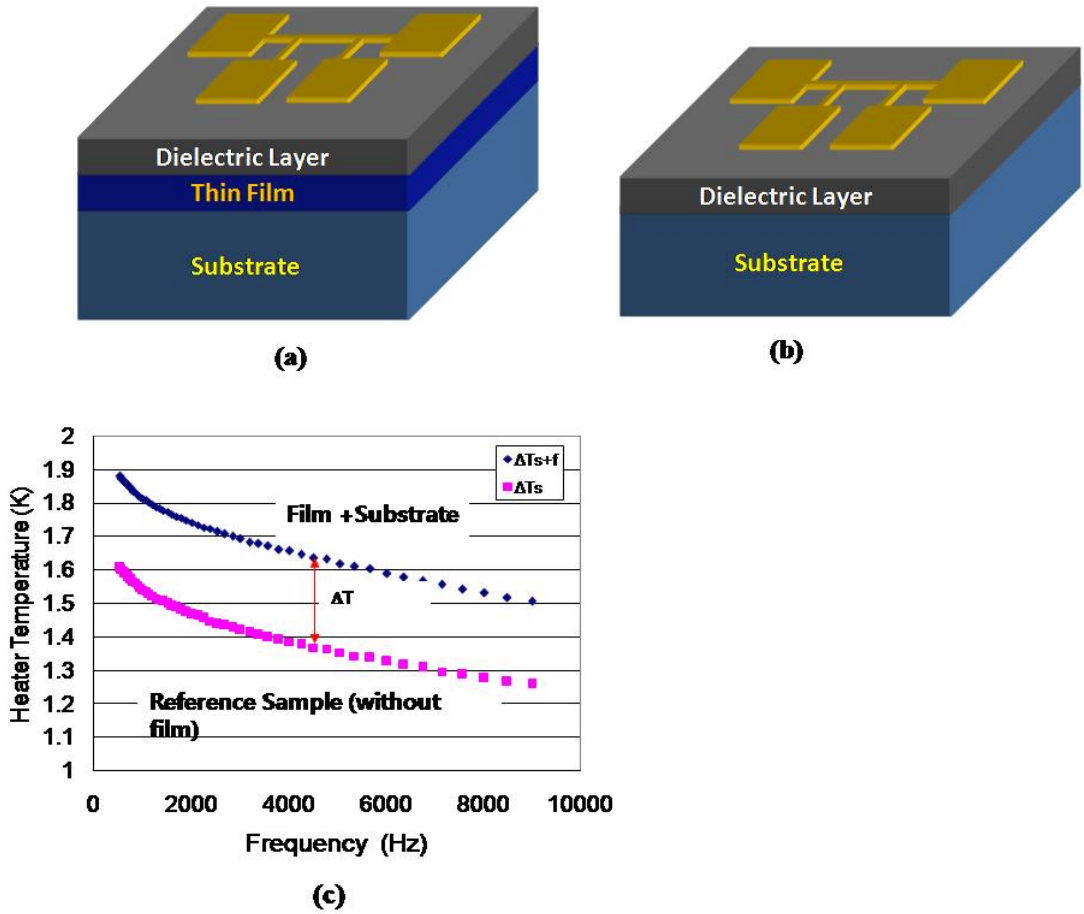

Figure 8. 3ω method for measuring *k* of thin film: (a) measurement on thin film sample; (b) measurement on reference sample without the film; (c) temperature difference from the two measurements is used to calculate the temperature drop across the film to determine its *k*.

1.3.3 Figure of merit

In 1909, ZT, known as Figure of Merit, is defined by Altenkirch. This is manifested in a steadily increasing figure of merit (ZT), where T is the temperature of operation, and Z= $S^2\sigma/K$ where **S** is the Seebeck Coefficient [in V/K], **σ** is the electrical conductivity [Ω-meter)], and **k** is the thermal conductivity [W/mK]. The efficiency of the thermoelectric material is directly related to ZT. For power generation, the efficiency is

$$\eta = \frac{T_h - T_c}{T_h} \frac{\sqrt{1 + Z\overline{T}} - 1}{\sqrt{1 + Z\overline{T}} + {T_c}/{T_h}}$$

and the coefficient of performance, the air-conditioning and refrigeration efficiency, is

$$COP = \frac{T_c}{T_h - T_c} \frac{\sqrt{1 + Z\overline{T}} - {T_c}/{T_h}}{\sqrt{1 + Z\overline{T}} + 1}$$

where T_h is the hot junction temperature, T_c is the cold junction temperature, and $\overline{T}$ is the average temperature of the T_h and T_c [2].

For higher ZT value, there are three requirements to meet. First, the Seebeck coefficient should be large enough to have large thermoelectric voltage. Second, the electrical conductivity should be large so that enough charge carriers can be transported. Third, the thermal conductivity should be low enough so that it maintains a thermal

gradient between junctions. However, it's not easy to have satisfying conditions for these three properties in one sample. As known, high electrical conductivity induces high k_e (thermal conductivity by electron transport) and possibly low Seebeck coefficient due to high carrier concentration. So, many research groups are trying to optimize these properties to maximize ZT values.

It is commonly accepted that a high ZT > 1 would result in thermoelectric materials useful for various applications such as heat recovery and space power applications, and ZT > 4 would simulate significant technology replacement in devices such as power generators and heat pumps.

1.4 Recent thermoelectric materials development

Since the 1960s, there have been tremendous efforts to find new thermoelectric materials. As a result, many new thermoelectric materials were identified such as Bi_2Te_3, SiGe, PbTe, CO_4Sb_{12}, and so on [2]. Many of these materials are alloys because their ZT values could be increased by reducing the thermal conductivity due to phonon scattering by atomic mass variations in alloy lattice structures. However, the alloys found during the three decades could not overcome the barrier of ZT=1 until it was found [3,4] that nanoscale dimensional restriction can lead to a much enhanced efficiency over traditionally used bulk alloy thermoelectric materials. In lower dimensions, abrupt peaks in the density of states (DOS) are observed (Figure 9), which can be correlated to an increased *S*. For example, in zero-dimensional quantum wells, or one dimensional nanowires the DOS becomes much more peaked than in the 3-dimensional bulk materials, at lower energies. In addition to an increased *S*, increased DOS leads to a higher

electrical conductivity (σ), which contributes to the figure of merit. Additionally, in lower dimensional structures, the lattice conductivity (k_{latt}) is proportional to the mean free path (l_{mfp}), which can be considerably reduced to below the phonon wavelength in confined structures such as nanowires. Thus, in nanoscale thermoelectric materials, it becomes possible to reduce the lattice thermal conductivity and increase the power factor ($S^2\sigma$) at the same time. Substantial R&D effort has been given toward the improvement of ZT values using these nanostructure advantages.

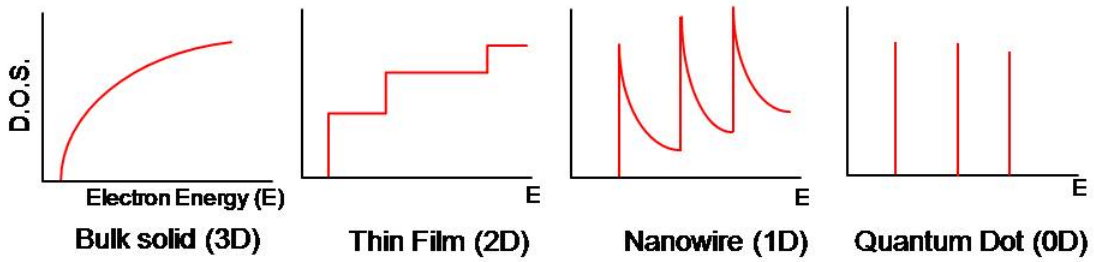

Figure 9. Electronic density of states for a bulk solid crystalline semiconductor, a 2D thin film, a 1D nanowire, and 0D quantum dot (from left).

During the past decade, several groups have reported enhanced ZT in superlattices such as Bi_2Te_3/Sb_2Te_3[5], SiGe/Si and $PbSe_{0.98}Te_{0.02}$/PbTe quantum dots[6]. The use of smaller diameter Si nanostructures [11-13] and defect engineering of Si, Bi_2Te_3-based, and other thermoelectric materials [7-10] to control electrical behavior and reduce thermal conductivity [13-16] have received much attention in recent years [17-27]. Figure 10 shows some remarkable enhancements in the figure of merit ZT that were recently made.

The superlattice structures can provide high ZT values. However, such thin film structures are not suitable for handling large amounts of energy because of the very small volume of thermoelectric material, small temperature gradient across the small material thickness, and the high cost of fabricating thin-film based materials on substrates. Therefore, there is a clear need for new, improved nanostructured bulk thermoelectric materials with high ZT values.

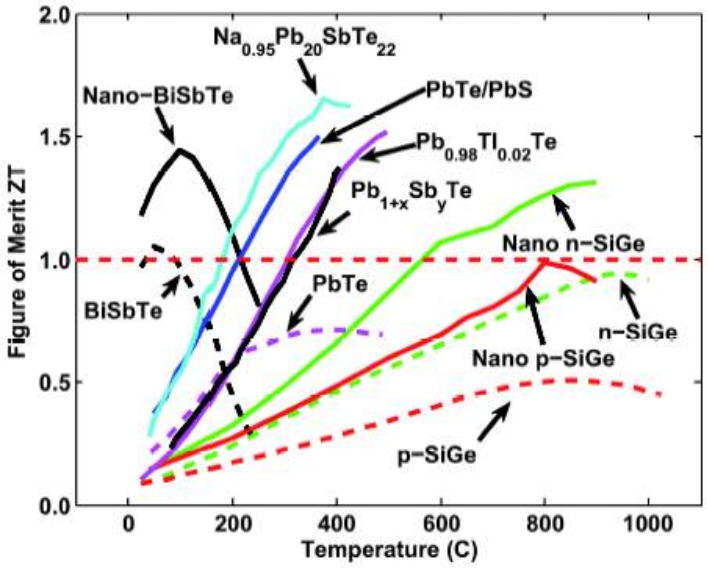

Figure 10. Figure of merit ZT of current state of the art thermoelectric materials versus temperature. The dashed lines show the maximum ZT values for bulk state of the art materials, and the solid lines show recently reported ZT values, many of which were obtained in bulk nanostructured materials [26].

CHAPTER 2: Fabrication of nanostructure

2.1 Introduction

In chapter 2, various new techniques and nanostructure generating systems that fabricate nanocrystalline structure in bulk sizes are described briefly.

2.2 Fabrication method concepts

2.2.1 Spark erosion method

Spark erosion has been used as a technique for producing research quantities of very rapidly solidified powders [28]. Current investigations have the objectives of extending the range of metals, alloys, and compounds prepared by spark erosion, determining the influence of electrical, mechanical, and chemical operating parameters on particle production rate, size distribution, composition, and microstructure, and increasing production rate and power efficiency. Thus far the work has demonstrated that spark erosion is a versatile and economical method for producing powders of a large variety of materials. The more noteworthy features of the process are the wide range of applicable materials and the small sizes of particles obtained.

For the case of thermoelectric materials, the ability of to conveniently produce micro particles at low fabrication cost, especially with extremely small grain size in the nanometer regime, is a significant advantage the spark erosion process. The technique is an efficient and powerful method to produce nano-grained TE material as the starting material for advanced processing in order to additionally increase lattice/grain defects and phonon scattering. Professor Berkowitz, one of the committee member, developed the spark erosion technique for metallic powder preparation about 2 decades ago when he was at General Electric [28].

When two electrodes are in close proximity in a dielectric liquid, an application of a voltage pulse can produce a spark discharge between them. Some of the energy in the spark discharge is transferred to the electrodes resulting in the heating of highly localized regions on the electrodes. If the regions are heated above their melting temperature, molten droplets or vaporized material may be ejected from the electrodes. Particles are produced by the freezing of the droplets in liquid. During the 1940's spark erosion was developed from the technology of electric discharge machining (EDM) in the Soviet Union. Electric discharge machining has become a widely used method for machining complex configurations in hard and tough materials. Interests in increasing the efficiency of the EDM process have produced a number of investigations on the phenomena involved in spark erosion.

Nanocrystalline particles are prepared by Spark Erosion method as illustrated by the schematic description given below. Figure 11 schematically describes the essentials of the process. On the left are two electrodes immersed in a dielectric liquid and connected to a pulsed power source. When the field strength in the gap is sufficiently high, a spark is produced.

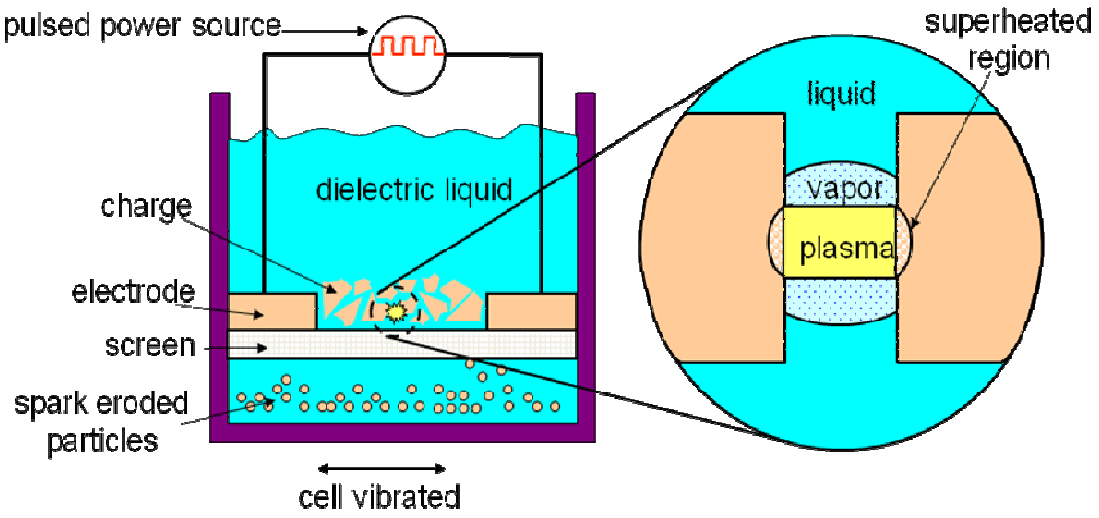

Figure 11. Spark Erosion Method Schematic Diagram [28]; Cell is vibrated to make and break spark gaps among charge pieces and electrodes.

The spark results from the breakdown of the dielectric fluid as depicted in the enlarged view of the reaction zone on the right-hand side of Figure 11. It is assumed that when the electric field is high enough there is substantial electron emission from the cathode. These electrons and others in the gap gain energy from the electric field and ionize molecules of the dielectric fluid producing more electrons and positive ions. A plasma channel of small diameter is established in approximately 10 ns after the electric field is applied. The temperature in the plasma channel has been determined to be very high, in excess of 10,000 K. As indicated in Figure 8, the high-temperature plasma column is surrounded by a sheath of vaporized dielectric that is confined by the relatively

incompressible liquid. Thus the pressure in the plasma column can be as high as 280 MPa. Figure 12 shows Bi-Sb-Te TE material charges in a cell for spark erosion process.

Figure 12. Bi-Sb-Te TE material charges (in a cell) for spark erosion process.

The temperature at the electrodes depends on the transfer of the kinetic energies of the electrons and ions to the anode and cathode, respectively. Since the mobilities of electrons are much higher than the mobilities of ions, short spark durations favor anode wear. The temperature of the locally heated regions of the electrodes is raised above the usual boiling point of the metal because of the pressure exerted by the plasma channel on this region. With the rapid decrease of pressure as the spark collapses at the end of the voltage pulse, the superheated regions boil violently, ejecting molten droplets and vapor into the dielectric liquid (in the case of TE materials processing, dodecane and water

were used as the dielectric fluid). Mechanisms other than the violent boiling of superheated regions may also contribute to erosion.

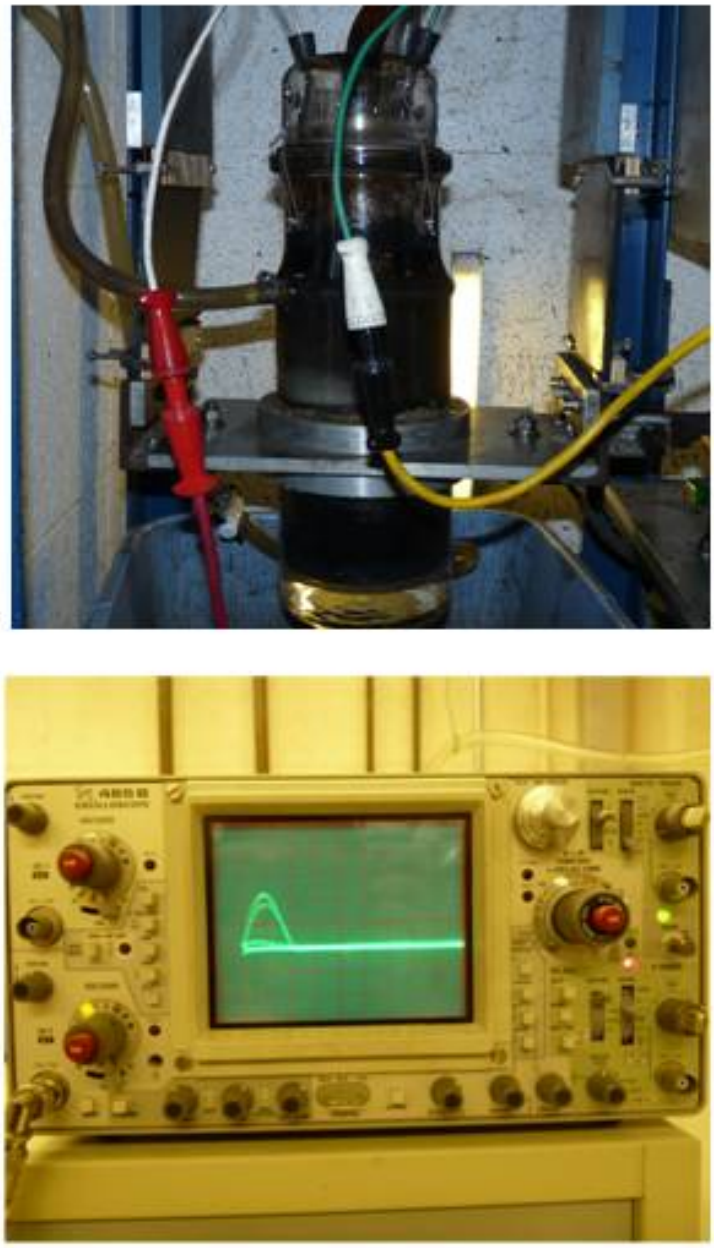

Figure 13. Spark erosion facility at UCSD. The TE material cell inside a dielectric liquid (up) and spark waves observed in oscilloscope (down). The dielectric liquid used here is dodecane ($C_{12}H_{26}$).

Figure 13 shows the spark erosion facility at UCSD (upper image). In spark erosion, many microparticles of Bi-Sb-Te alloy particles accumulate at the bottom of dielectric liquid vessel. The spark wave that occurs between thermoelectric charges and electrodes is shown in Figure 13 (lower image). Sparks for fabrication of nano-grained TE particles can be actuated more than 50 times per second (50 – 60 Hz).

2.2.2 Ball milling powder method

Ball milling method is a simple but powerful method to fabricate thermoelectric samples. Many research groups are using a ball milling method to prepare a sample. In this thesis, ball milling was performed using a Fritsch “Pulverisette7”, a high energy ball milling system, to produce nano-size BiSbTe alloy powders. The bowl and balls are made of Zirconium oxide. The Pulverisette7 rotates the main disk and the grinding bowls independently to maximize grinding performance. The speed and the number of balls are optimized in the project to produce appropriate characteristics of the powders. The powder is held in an Argon gas filled glove box and milling bowls to prevent oxidation of the powders. Figure 14 shows the sketch of the ball motion inside the planetary ball mills. The rotation of the grinding bowl and the movement of the supporting disk are opposite in direction to maximize the grinding efficiency.

A surfactant assisted ball-milling was also performed using a SPEX-8000 ball mill (Figure 15). Heptane (99%) was used as the ball-mill medium and Oleic Acid (99%) was used as the assisting surfactant. In SPEX 8000 the bowl is shaken along three independent axes, thereby ensuring a chaotic motion of the balls. The surfactant assisted ball milling for 10hours produced fine particles less than 50nm diameter size. The Oleic

Acid plays an important role in producing fine particles because it decreases particle agglomeration during milling.

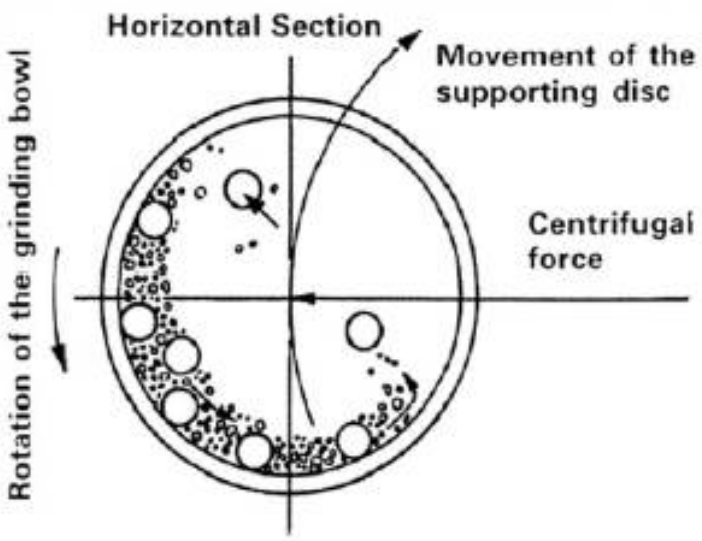

Figure 14. Sketch of the ball motion inside the planetary ball mills [2007 Manual].

Figure 15. SPEX 8000 Vibratory ball mill system (from SPEX catalog).

2.2.3 Swaging method

One efficient way of exploiting quantum confinement to achieve high thermoelectric figures of merit is to fabricate sub-10nm (and preferably sub-5nm) diameter thermoelectric material along the electric current flow direction with the nanowires spaced apart and physically separated by an electrical insulator material matrix. These one dimensionally elongated and aligned thermoelectric nanowire arrays are desirable since the added lateral electronic and thermal (i.e., phonon) constriction provides an additional degree of quantum confinement in the lateral direction. Such nanowire confinement effect becomes pronounced only if the nanowire diameter is about or less than the Bohr radius, which depends on the effective mass of carriers and dielectric constant of the material, and is below ~ 5-10 nm. Obtaining such sub-10 nm thermoelectric wires is not easy, and thus requires novel processing approaches.

Uniaxial or unidirectional deformation (such as swaging, wire drawing) and slicing will be utilized to assemble such one-dimensionally and anisotropically nanostructured thermoelectric structures at the desired macro-scale sizes. The principle of the processing scheme is outlined in Figure 16. The uniaxial plastic deformation reduces the cross-sectional diameter of the thermoelectric particles or fibers separated by electrically or thermally insulating material causing them to elongate inducing anisotropic alignment. The thermoelectric material is packed in a copper tube with either ¼ inch or 3/8 inch outside diameter. Optionally the use of aluminum oxide or silicon oxide nanoparticles (~10 – 30nm) was also explored, which may assist in separating the TE

alloy grains from each other for maximum nano-effect, but may contribute to reducing volume fraction of the TE alloy in the composite.

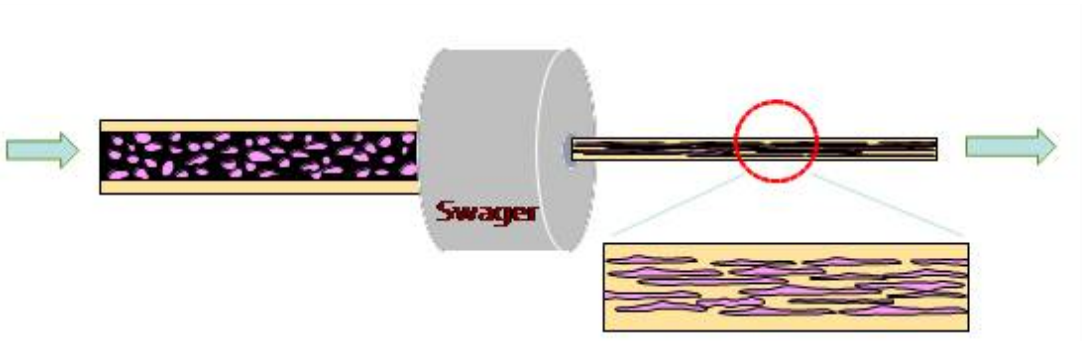

Figure16. Schematic illustration of the dimensional reduction of TE alloy particles in copper jacket using a swager machine.

2.2.4 High strain rate deformation

Hopkinson Bar Impact deformation with strain rate as high as ~2000 in/in/sec over ~200 microsec (as compared to the strain rate of ~1/sec for sledge hammer hitting) is utilized in this research for the following purposes.

i) To provide high strength compaction for increased ZT through reduction of pores and empty spaces in the TE material volume,

ii) To flatten the thermoelectric material grains/particles to smaller dimensions for enhanced boundary phonon scattering and higher ZT.

iii) More importantly, the extremely high strain-rate utilized for plastic deformation is likely to substantially increase the amount of nano-defects in the thermoelectric material with minimal annealing-out of the defects. Such defects in

thermoelectric materials are known to increase phonon scattering and reduce thermal conductivity, which results in an enhanced ZT figure of merit. High strength impact test of Hopkinson bar is performed at room temperature and Liquid Nitrogen temperature (-196 °C) as illustrated in Figure 17. A lower temperature (or a cryogenic temperature) plastic deformation often introduces mechanical twinning defects due to the lack of sufficient slip systems for dislocation cross-slip together with minimal annealing-out of defects under such a low temperature environment. The removal of defects such as dislocations, point defects, and twin boundaries are all suppressed by such deformation mode. It is for these reasons that we investigated low temperature, high-strain-rate deformation. The low temperature deformation such as that at liquid nitrogen temperature can be cost-effectively performed in air using insulating styrofoam type channel protection without using any cryostats.

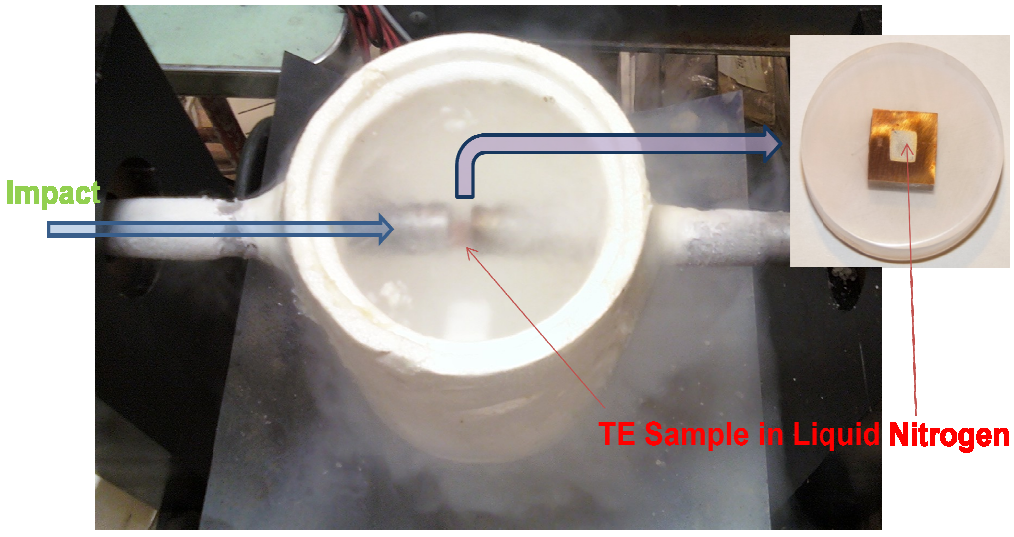

Figure 17. High strain rate impact test with Hopkinson bar is performed in Liquid Nitrogen (-196 °C).

2.2.5 Spark plasma sintering (SPS)

In a high densification process, it is favored to maintain the grain size of the powders to obtain high ZT values. Traditionally, hot pressing is widely used to compact powder into bulk materials. However, it has been necessary to apply high temperature to avoid pores inside samples in hot pressing process, which results in grain growth. The Spark plasma Sintering (SPS) is one of the techniques that can solve this problem.

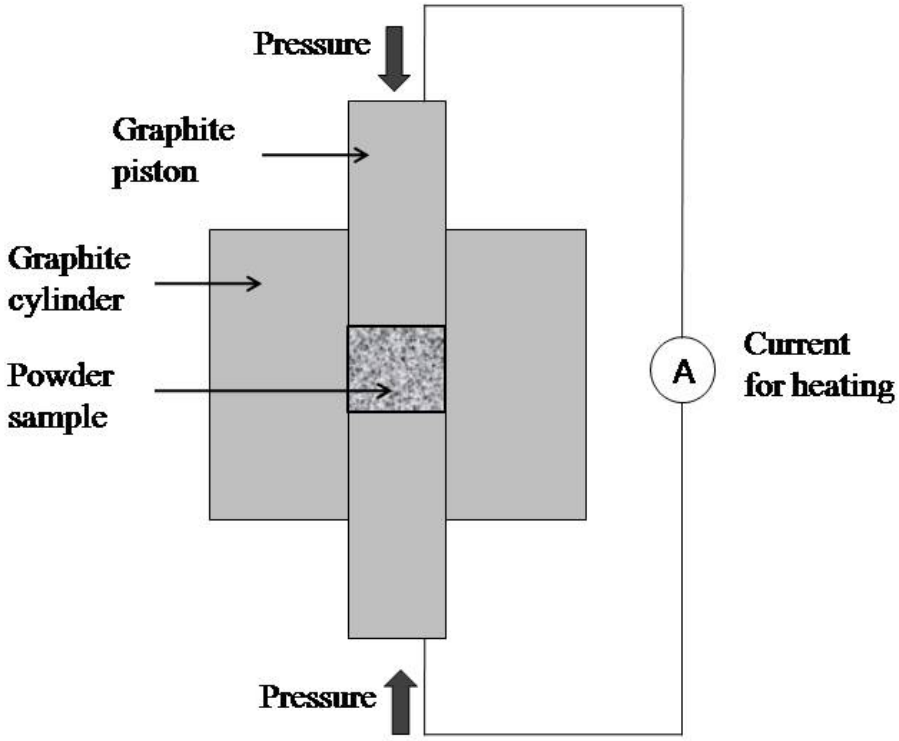

Figure 18. Schematic of Spark Plasma Sintering (SPS).

The SPS system is a unique method that combines mechanical pressing and electrical heating. In this process, the mechanically ground or spark eroded TE powders are placed inside a graphite cylinder and then compressed with a DC current along the

powders and graphite cylinder. The advantage of the SPS system is the rapid densification in a very short time compared to the hot pressing process. To maximize ZT value, the temperature, pressure and holding time are optimized. Figure 18 shows the schematic of Spark Plasma Sintering (SPS).

2.2.6 Rapid Pulse Sintering (RPS)

The Rapid Pulse Sintering (RPS) system is designed to enhance the advantage of spark plasma sintering (SPS) system. SPS has many advantages over traditional hot pressing method but it still uses heat from the graphite cylinder surrounding the sample.

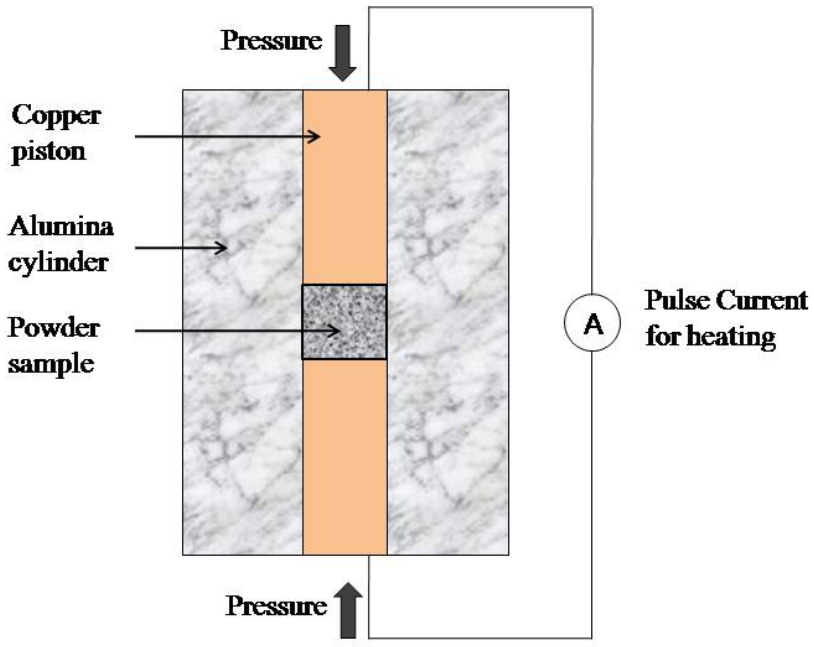

Figure 19. Schematic of Rapid Pulse Sintering (RPS).

The RPS system uses only heat induced from the resistivity in the powder sample for densification. Because it has an electrically insulated surrounding cylinder made of alumina, all the current applied goes through the powder between the copper punches so that resistive heat along the powders is maximized. Figure 19 shows the schematic of Rapid Pulse Sintering (RPS).

CHAPTER 3. Experimental results and discussion

3.1 Swaging deformation process and results

The thermoelectric alloy was compacted in a metal jacket and uniaxially swage deformed as described below. $Bi_{0.5}Sb_{1.5}Te_{3.0}$ Spark eroded particles (10~50 μm average diameter polycrystalline particles with ~70 nm grain size) or ground particles (500 nm average diameter) are pre-compacted in hydraulic press machine (at 10,000 pounds pressure), Figure 20, to enhance starting density of TE powder inside the copper tube jacket. Either cylindrical compacts or rectangular compacts of TE alloy (with subsequent corner grinding to make the cylindrical TE fit into the geometry of the Cu tubing interior) were prepared.

Figure 20. $Bi_{0.5}Sb_{1.5}Te_{3.0}$ Powder and dies for pressing of TE powders with a force of up to 10,000 lbs.

Pressed powder compact is inserted into a 0.375 inch copper tube (3/8 inch) and its outside diameter is reduced down to ~0.125 inch (corresponding to ~90% deformation of reduction in area) using the swaging machine with appropriate series of dies as shown in Figure 21.

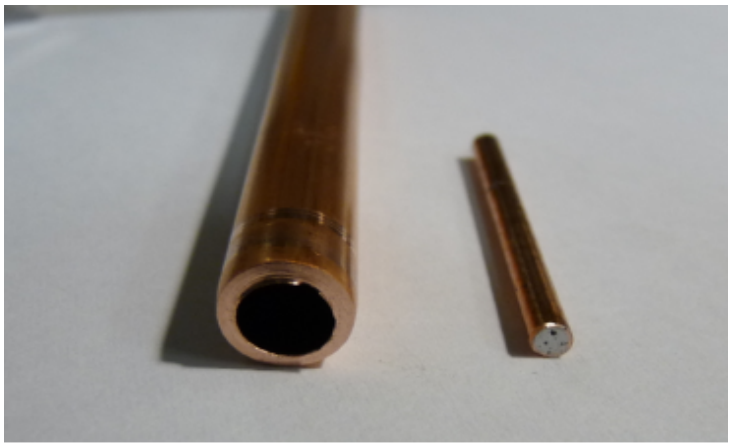

Figure 21. Starting 0.375 inch copper tube with compacted $Bi_{0.5}Sb_{1.5}Te_{3.0}$ powder and swaged rod down to 0.125 inch composite diameter.

Optionally the process of uniaxial plastic deformation by swaging (Figure 21, 22) was repeated to reduce the rod diameter and at the same time elongate the thermoelectric alloy particles for the ductile alloy types.

Figure 22. Swager machine for uniaxial elongation, and the swaging die that reduces the diameter of rods or tubes in the swager machine.

This elongated thermoelectric metal/alloy assembly structure can be rebundled in another larger metal tube and continued to be deformed as in Figure 23. A 0.25 inch copper tube is used for rebundling and reducing the size to 0.125 inch. This process has

been established for future utilization of severe deformation and significant diameter reduction of TE alloy nano-grains in the 0.2 – 5 nm regime to study the effect of nano diameter vs thermal conductivity, Seebeck Coefficient, electrical conductivity, and the resultant effect on the final ZT values. Starting with 70 nm grains (as in spark eroded $Bi_{0.5}Sb_{1.5}Te_{3.0}$ particles), four-times repeated deformation of 90% reduction area would lead to a reduction of diameter by a factor of (3 x 3 x 3 x 3) = 81, which would in principle produce a nanograin diameter of 0.9 nm, well in the size regime for a steep rise in ZT as the diameter is reduced. Eventually, TEM microscopy will be used to determine the nano-grain geometry and defects associated with such nano-grain forming deformation process. A scheme of measuring or numerically estimating thermal conductivity and ZT in such fabricated nanostructures may be a challenging but exciting physics and experimental task, which may lead to deeper fundamental understanding of the TE materials behavior.

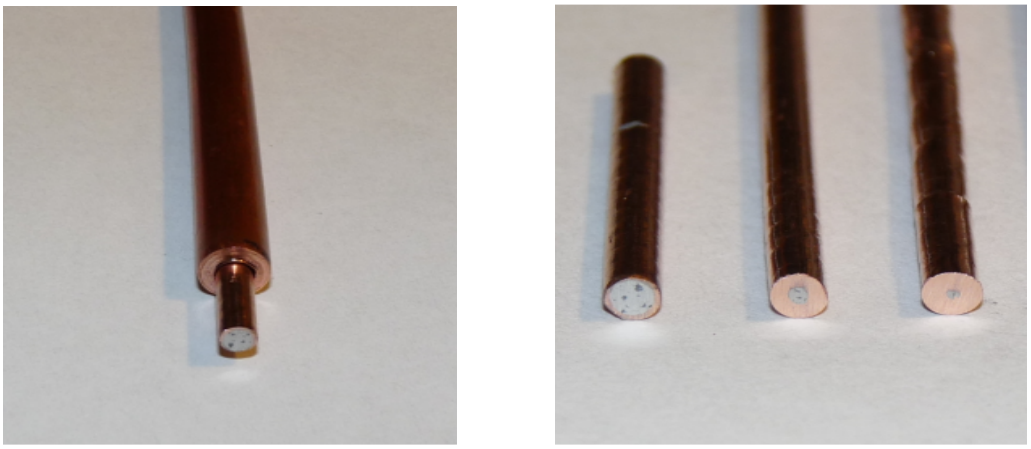

Figure 23. Uniaxially elongated thermoelectric alloys inside copper tubes by rebundling and swaging (left picture). Elongated thermoelectric alloys tubes with 1/3 diameter, 1/6 diameter, 1/12 diameter and 1/24 diameter compared with starting 0.375 inch tube (right picture) (From left).

After uniaxial elongation deformation, the metal jacket can be removed by a chemical etching process if needed. In the case of the copper metal jacket, a ferric chloride solution was used as the etchant to produce a bare TE material as shown in Figure 24.

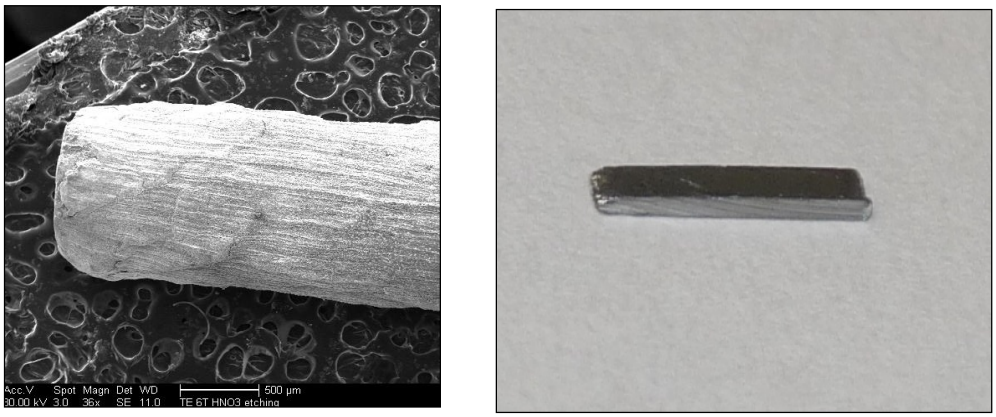

Figure 24**.** SEM swaged and Cu-etched sample fixed on an adhesive tape (Left) and polished sample (right).

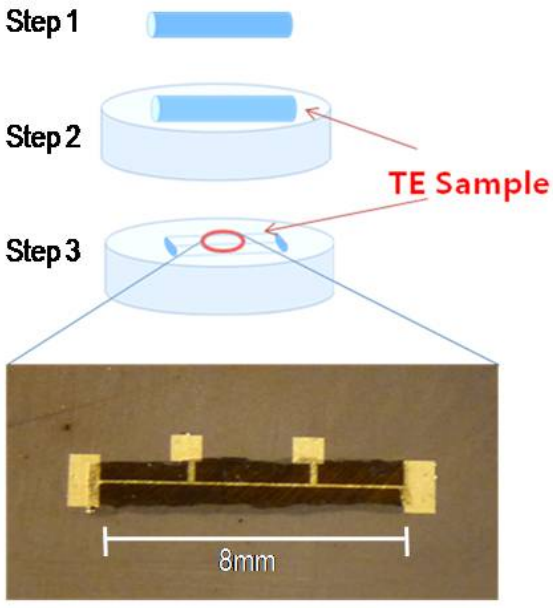

Figure 25. Schematics of swaged sample preparation for thermal conductivity by 3ω method

Figure 25 shows the schematics of swaged sample fixed inside epoxy and polished for photolithography to measure the thermal conductivity by 3ω method. A platinum strip is used as a heater and thermometer. Typically the strip width is 30 µm, the length is 8 mm, the distance between the inner pads is 4 mm and the thickness is 400 nm.

Some of the TE rods were also annealed in a furnace at ~500^{o}C, slightly below the melting point of the $Bi_{0.5}Sb_{1.5}Te_{3.0}$ alloy. An argon gas was continuously supplied to the tube furnace to minimize oxidation of the $Bi_{0.5}Sb_{1.5}Te_{3.0}$ alloy samples. Swaging deformation method is combined with the high strain deformation method described in the previous chapter to maximize the particle defects.

Shown in Figure 26 is some preliminary thermal conductivity values measured for the processed Bi-Sb-Te alloy samples using the 3-ω method described earlier. The spark eroded + Cu jacket swaged + higher temperature (610^{o}C) annealed sample in the composite state (sample #1) gave a lower ***K*** of ~1.0 W/m-K. However this sample was fragile and not dense with no impact deformation given to densify the material within the Cu jacket. The bulk Bi-Sb-Te + impact deformed sample (#D) gives a ***K*** value of ~1.1 W/m-K. When the deformation of the bulk sample is conducted at cryogenic temperature of -196^{o}C (sample #G)), about a 20% further reduced ***K*** of ~0.9 W/m-K is obtained. The spark eroded (nano-grained) + impact deformed samples (#P,Q,R) exhibit a much lower ***K*** value of ~0.824 W/m-K for the sample #P and slightly higher values for #Q and #R.

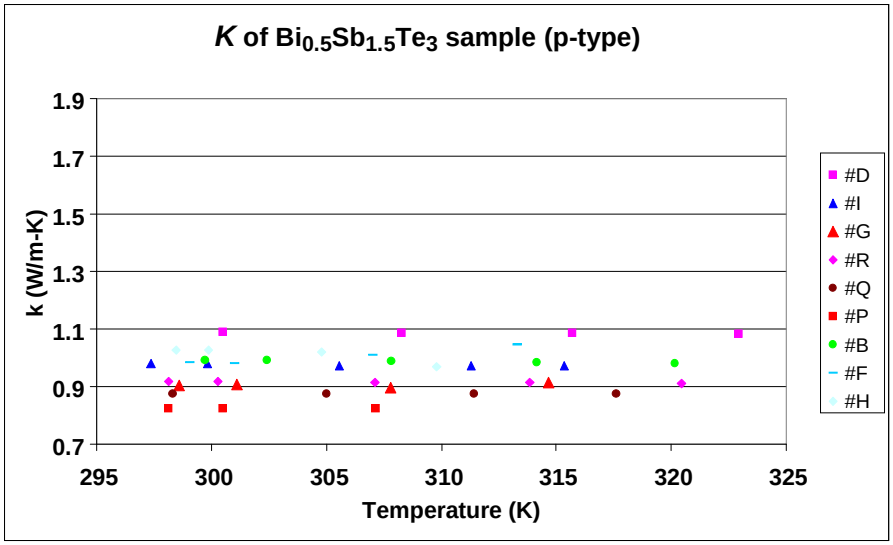

#A~C: Spark Eroded Powder + 10,000lb Pressed + Hopkinson Compaction
#D~F: P-Type Bulk + Hopkinson Compaction
#G: P-Type Bulk +Nitrogen Liquid(-196C) + Hopkinson Compaction
#H~I: P-Type Bulk+Shrinking tube + Hopkinson Compaction (Thin disk)
#J~K: Spark Eroded Powder + 10,000lb Pressed + Shrinking tube + Hopkinson Compaction (Result:Thin disk)
#P~R: Spark Eroded Powder + 10,000lb Pressed + Cu tube swaged + Hopkinson Compaction from side
#1: Spark Eroded+ Cu jacket swaged + 610°C/3 minute annealed as a Cu jacketed composite state (Fragile and not dense)

Figure 26. Thermal conductivity values (at room temp) for various $Bi_{0.5}Sb_{1.5}Te_3$ alloy samples processed with spark erosion and/or impact deformation.

Table 1. Comparative thermoelectric behavior for high strain impacted spark erosion powder of Bi-Sb-Te alloy (~25 μm powder with 70 nm nano-grains), MIT/BC's ground+hot pressed Bi-Sb-Te alloy and ingot bulk with same composition

Fabrication Method	Material Composition	σ (S/m)	*S* (μV/K)	*K* (W/mK)	ZT (300K)
Ingot Bulk	$Bi_{0.5}Sb_{1.5}Te_{3.0}$	1.0E+05	210	1.4	1.0
Ball mill+H.P. [15]	$Bi_{0.5}Sb_{1.5}Te_{3.0}$	1.2E+05	188	1.1	1.2
Spark erosion + Impact deformation (Sample #P)	$Bi_{0.5}Sb_{1.5}Te_{3.0}$	1.0E+05	199	0.82	1.4

The ZT values for the sample #P (~25 μm powder with 70 nm nano-grains + 10,000 lb pressed + Cu jacket swaged + Hopkinson Bar Compaction (high-strain-rate deformed) is calculated. With the Seebeck coefficient of S = +199 μV/K, electrical conductivity of s = 1.0 x10^5 (S/m), and the thermal conductivity of K= 0.82 (W/mK) at 300K, the ZT value is calculated to be ~1.4. This is a quite high value of thermoelectric figure of merit. This value is compared in Table 1 with the best reported ZT value by the MIT/BC group [15] with the ZT=~1.2 at room temperature.

3.2 Spark erosion process and results

The spark erosion fabricated particles are generally spherical and 1 µm - 75 µm in diameter within which polycrystalline grains (or amorphous alloy material depending on specific alloy compositions) exist. This particle morphology shown in Figure 27 for the Bi-Sb-Te alloy is characteristic of spark-eroded particles. Although the dielectric fluid used, dodecane, is a hydrocarbon liquid ($C_{12}H_{26}$), there was no noticeable carbon contamination in the $Bi_{0.5}Sb_{1.5}Te_{3.0}$ particles fabricated by spark erosion.

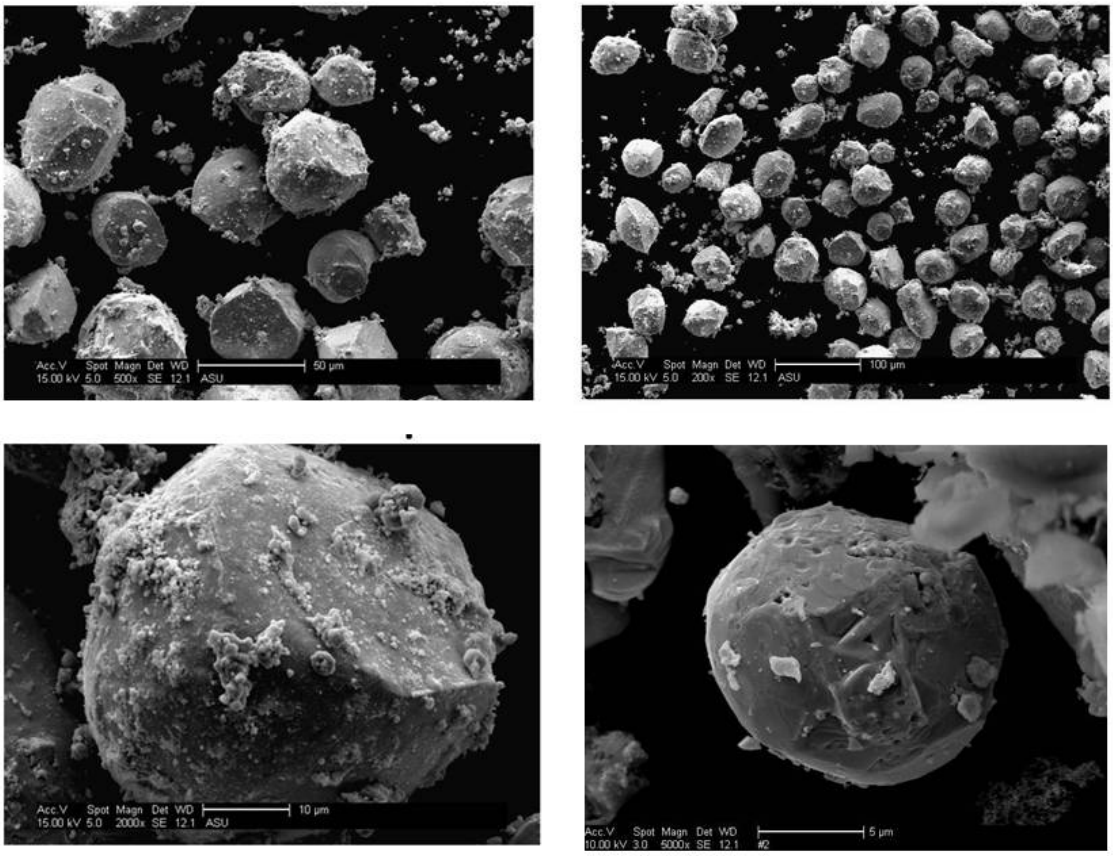

Figure 27. Spark erosion process produces roughly 10~50 µm diameter particles, with each particle containing nano-grains of ~70 nm average size.

Table 2. Composition ratio of spark eroded particles of Bi-Sb-Te

		25-53 µm					
Spherical Particles		Particle 1	Particle 2	Particle 3		Average	SD
At%	BiM	11.46	12.11	11.37		11.6	0.4
	SbL	26.50	28.05	29.54		28.0	1.5
	TeL	62.04	59.83	59.10		60.3	1.5
Nonspherical Particles		Particle 1	Particle 2	Particle 3		Average	SD
At%	BiM	12.42	11.35	5.14		9.6	3.9
	SbL	27.88	25.66	28.94		27.5	1.7
	TeL	59.70	62.99	65.92		62.9	3.1
		53-75 µm					
Spherical Particles		Particle 1	Particle 2	Particle 3		Average	SD
At%	BiM	5.14	11.75	12.77		9.9	4.1
	SbL	32.10	27.62	27.09		28.9	2.8
	TeL	62.76	60.63	60.14		61.2	1.4
Nonspherical Particles		Particle 1	Particle 2	Particle 3		Average	SD
At%	BiM	12.27	11.26	8.38		10.6	2.0
	SbL	28.49	25.49	25.61		26.5	1.7
	TeL	59.24	63.25	66.01		62.8	3.4

The spark erosion method produces 10~50 µm average diameter thermoelectric particles (Figure 27) in a relatively short period of time with the particles themselves consisting of ~70 nm diameter grains. The internal structure is analyzed via X-ray diffraction (XRD) method. From the XRD peak widths, grain size is expected to be between 50-100 nm (due to line broadening). The peaks represent the desired Bi-Sb-Te phase, with the average composition determined to be very close to nominal $Bi_{0.5}Sb_{1.5}Te_{3.0}$ alloy composition.

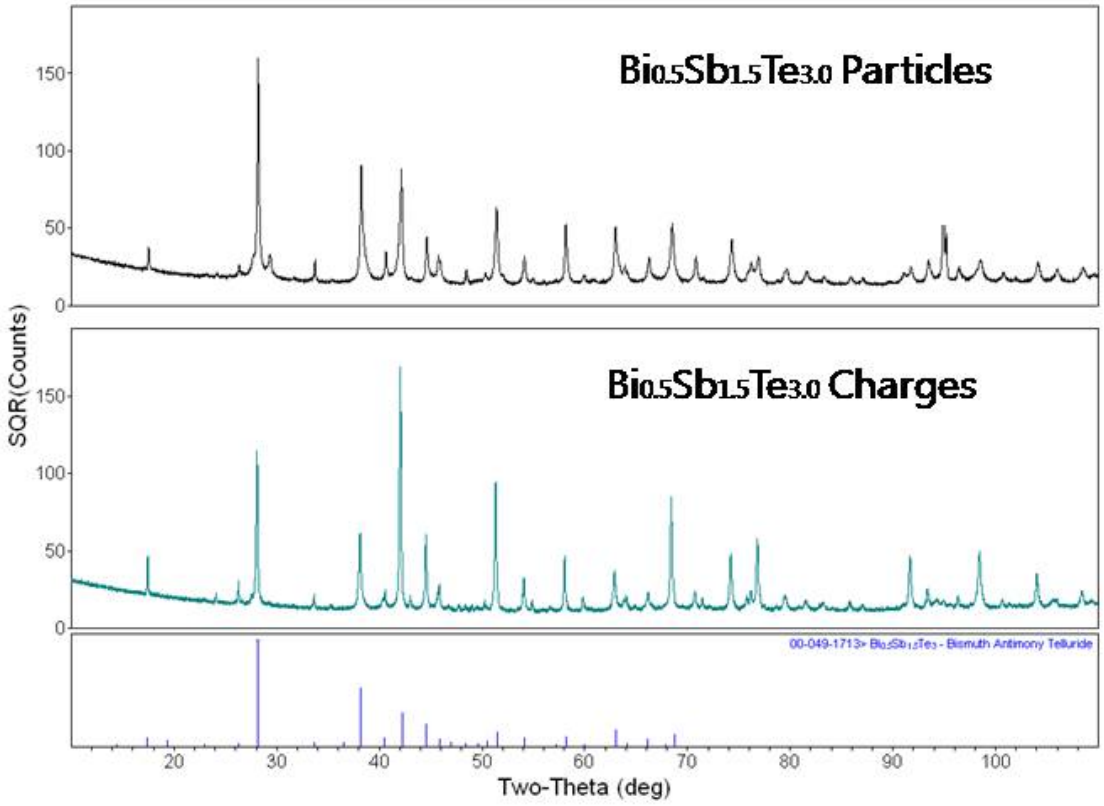

Figure 28. XRD Peak fitting results of spark eroded particles (top) to the grain sizes of 26 nm ~92 nm (average 67nm) compared with Charge (Bulk) result of grain size of > 100nm.

As is well known, X-ray peak broadening can be utilized for estimation of grain size of the material. XRD analysis software 'JADE' yielded the average size of 67 nm based on the XRD pattern shown in Figure 28. This means spark erosion method is a very effective tool to produce thermoelectric nanocrystalline particles. Liquid processing such as melt spinning of molten metals/alloys fabricates thin ribbons of amorphous or nanocrystalline material. However, such a melt processing is slow and expensive. There are no other convenient methods of producing such a fine grain size. It is believed that

the “Spark Erosion” method that we utilize can be a very viable industrial production technique for nano-grained thermoelectric materials.

3.2.1 Nano-composite by the Spark Erosion Method

The spark erosion method can be utilized to produce nano-composite particles. In one of our experiments, H_2O with SiO_2 particles of ~4 nm size (15% weight concentration) is used as dielectric liquid during spark erosion.

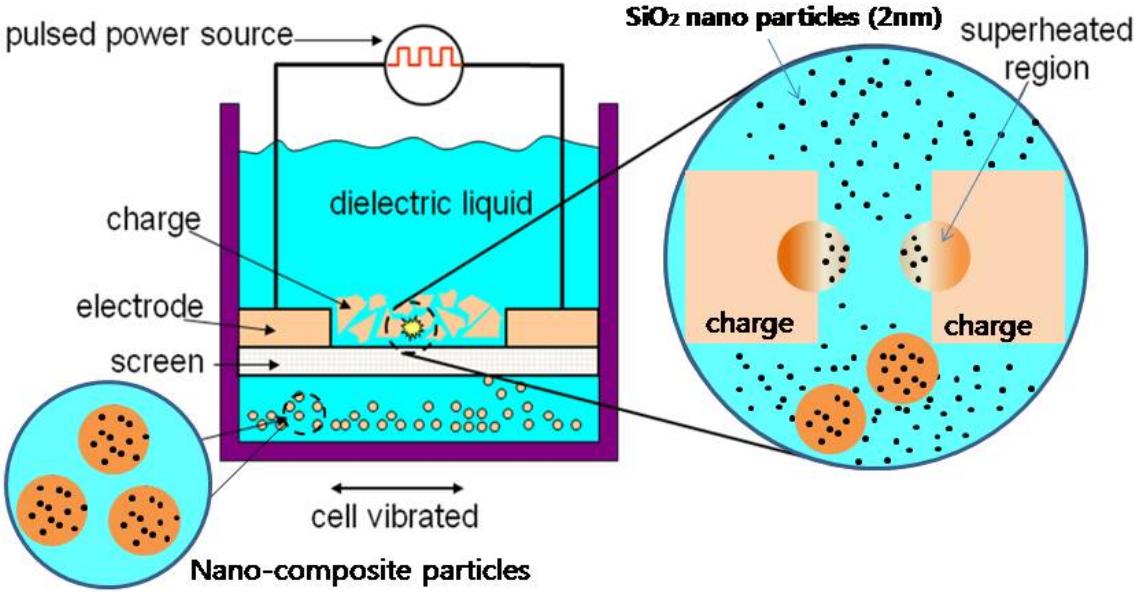

Figure 29. Schematic of Nano-composite particle fabrication by the spark erosion method: The dielectric colloidal liquid (H_2O base) containing nano particles (SiO_2 of 4 nm size) is used to produce the nano-composite particles of $Bi_{0.5}Sb_{1.5}Te_{3.0}$ spark eroded in a colloidal solution of 4 nm SiO_2 (15% wt) in H_2O.

The nano-particles of SiO_2 are thus embedded inside spark eroded Bi-Sb-Te particles, which may be utilized for creating a new TE alloy structure consisting of a Bi-Sb-Te

matrix with uniformly dispersed phonon-scattering nanoparticles. Such a structure is much more desirable than the traditional structure of foreign nanoparticles decorating the outside (surface) of Bi-Sb-Te particles or grains. The schematic diagram in Figure 29 describes the nanocomposite particles produced by the spark erosion method.

EDXA (energy dispersive X-ray analysis) was performed using a very small, 100 nm diameter detection beam on a clean area of the $Bi_{0.5}Sb_{1.5}Te_{3.0}$ spark eroded powder surface (see the inset in Figure 30), which was synthesized in the dielectric solution of H_2O containing 4 nm SiO_2 nanoparticles (15% wt). The EDXA data indicates that there is SiO_2 incorporated into the spark eroded Bi-Sb-Te particle.

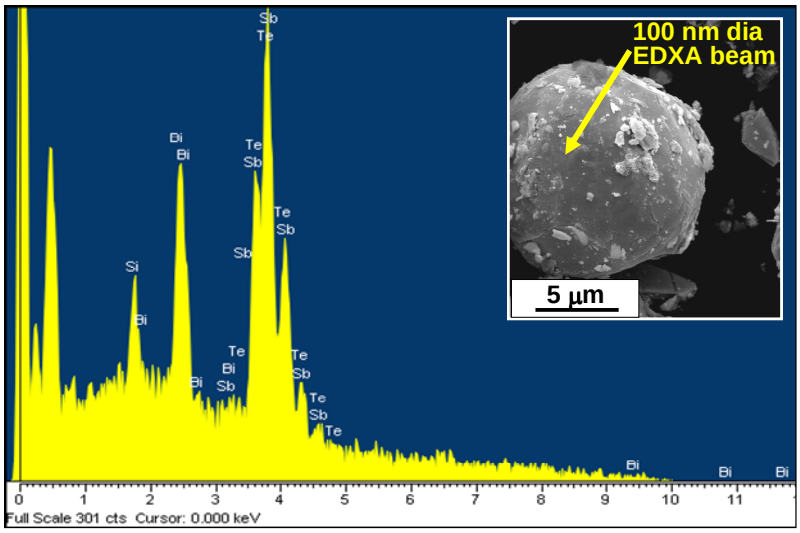

Element	App Conc.	Intensity Corrn.	Weight%	Weight% Sigma	Atomic%
Si K	0.02	1.2905	1.92	0.24	8.57
Sb L	0.27	0.9919	30.64	1.55	31.58
Te L	0.56	1.2195	50.53	1.60	49.69
Bi M	0.14	0.8987	16.91	1.22	10.15
Totals			100.00		100.00

Figure 30. EDXA (Energy-dispersive X-ray analysis) of nano-composite particles: the composition ratio shows the evidence of SiO_2 nanoparticles inside a 5 µm diameter spark-eroded $Bi_{0.5}Sb_{1.5}Te_{3.0}$ particle.

The EDXA data shown as a table in Figure 30 strongly indicates that SiO_2 nano-particles are embedded in Bi-Sb-Te spark eroded particles. Further analysis of microstructure by careful TEM is required to directly confirm the presence of 4 nm SiO_2 nanoparticles dispersed within the grain of micrometer sized Bi-Sb-Te particles.

3.2.2 Nano-grain structure in the Spark Eroded Bi-Sb-Te alloy particles

The spark erosion of $Bi_{0.5}Sb_{1.5}Te_{3.0}$ alloy in the presence of SiO_2 nanoparticle-containing dielectric solution (H_2O) produced extremely fine grain sizes of average nanoscale grain diameter or width of 20~50 nm within the spark eroded microparticles as shown in Figure 31.

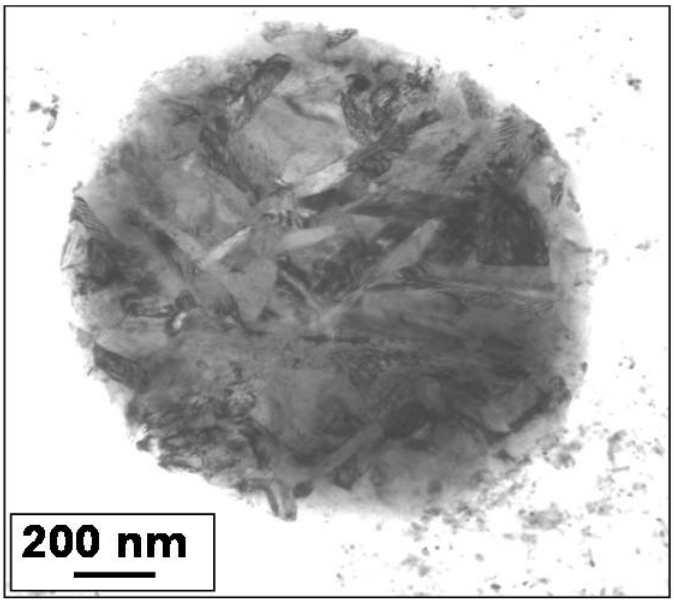

Figure 31. Cross-sectional TEM of spark erosion synthesized Bi-Sb-Te–(SiO_2) alloy microparticle, which shows an average nanoscale grain diameter or width of 20~50 nm.

Some grains are isotropic in shape but many grains appear to be somewhat elongated. The $Bi_{0.5}Sb_{1.5}Te_{3.0}$ alloy powders were mounted in epoxy sample and cross-sectioned to see the microstructure within each microparticle. The presence of 4 nm diameter SiO_2 nanoparticles may have minimized grain growth during the melting and rapid solidification process of spark erosion. The very large grain boundary surface area and associated defects in such nanograined thermoelectric materials can serve as phonon scattering centers to lower the thermal conductivity, and hence increase the ZT value.

3.2.3 Hollow thermoelectric particles by the Spark Erosion Method

If spark erosion is carried out in liquid nitrogen dielectric instead of H_2O or any other dielectric liquid, mostly hollow thermoelectric micorparticles of $Bi_{0.5}Sb_{1.5}Te_{3.0}$ are produced.

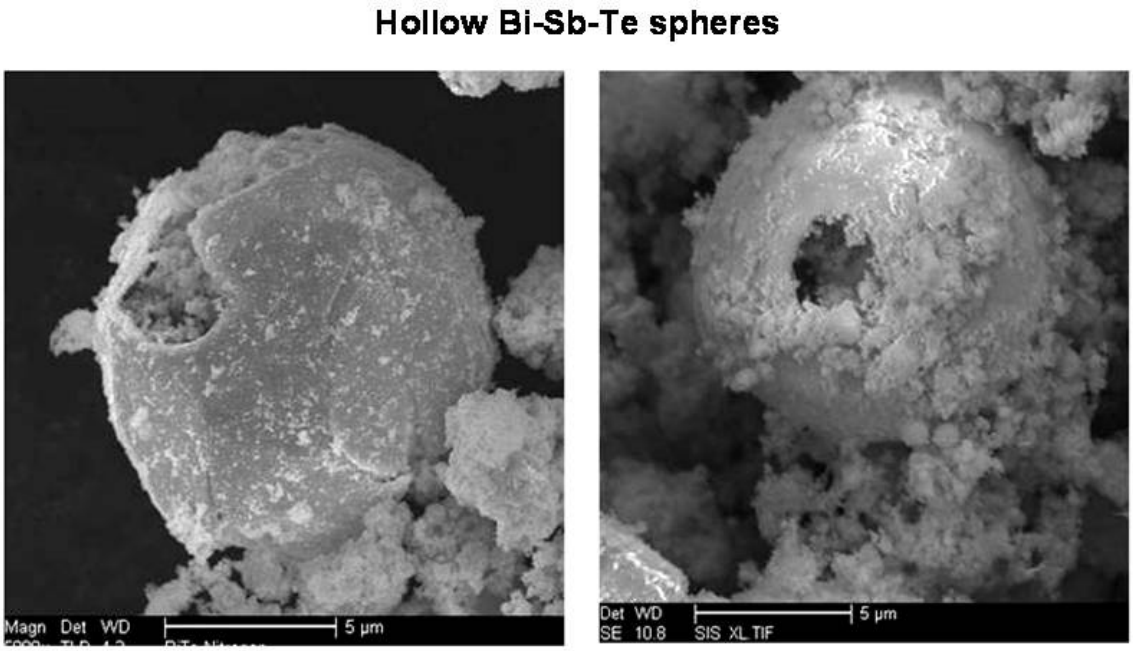

Figure 32. Hollow thermoelectric particles produced by the spark erosion in liquid nitrogen shown in the SEM micrographs with the nanowall thickness of 10 ~20 nm.

The SEM micrographs of the microparticle in Figure 32 were taken from spark eroded Bi-Sb-Te particles that were intentionally ground to partially fracture them for the purpose of showing the hollow nature of the particles. Many of the Bi-Sb-Te microparticles were well rounded hollow particles with nitrogen gas trapped within and have no cracks or holes. These hollow TE particles exhibit nanowall thicknesses of only about ~10-20 nm as shown in Figure 32, and hence the Bi-Sb-Te material grain size is expected to be extremely small. Such a nanowall might present some interesting thermal, electrical, Seebeck and thermoelectric properties. One of the possible future studies is pulverizing these hollow spheres to produce ~10-20 nm thick flakes and decorating the surface with nanoparticles of SiO_2, Al_2O_3 or Ag followed by rapid pulse sintering to produce a thermoelectric bulk alloy that has a rather uniformly dispersed nanocomposite structure. These hollow thermoelectric spheres may also be considered for fabrication of ultra-light, or floatable thermoelectric materials and devices. These hollow TE particles can be used to lower the thermal conductivity and can help find many new applications.

3.2.4 “Nanowall” thermoelectric alloys

We have discovered that if we use liquid nitrogen, instead of water or dodecane as the dielectric liquid during spark erosion, we obtain a very hollow sphere of Bi-Sb-Te alloy as shown in Figure 32. The wall thickness of the hollow micro spheres appear to be only ~10 -20 nm. Such a small dimension of ~10 nm regime can substantially reduce the thermal conductivity of the thermoelectric alloy, thus enhancing the overall ZT characteristics.

Such hollow structure could be utilized for creating new nanostructures of thermoelectric alloys as illustrated in Figure 33. The hollow spheres of Bi-Sb-Te can be pressed and rapidly sintered (using "Rapid Pulse Sintering (RPS)" method developed in this research) to form a 3-Dimensional honeycomb structure, thus creating "Nanowall thermoelectric alloy". A necessary process for such honeycomb formation is the rapid sintering, which avoids coarsening of the nanowall structure into a thicker dimension.

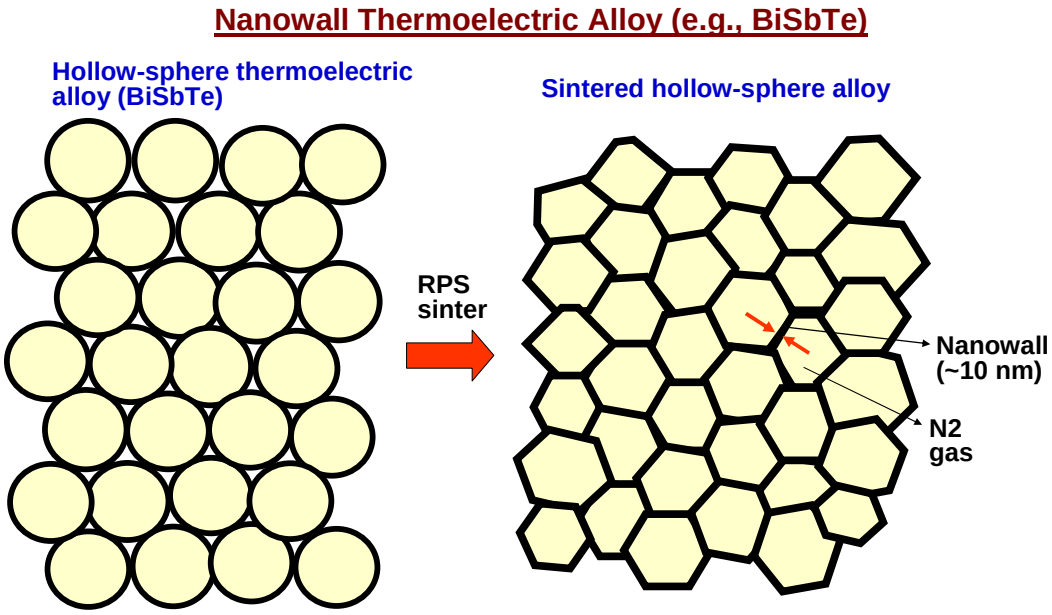

Figure 33. Schematic of the compression and rapid sintering of hollow sphere Bi-Sb-Te microparticles into 3-D network honeycomb structure of "Nanowall thermoelectric" alloy.

Shown in Figure 34 is an alternative configuration of thermoelectric alloy consisting of hollow compartment (squashed honeycomb). Such a structure can be made by plastic deformation of the honeycomb structure, either at room temperature or at high temperature (e.g., by heating to 400 ~500°C below the melting temperature of the Bi-Sb-

Te alloy where the Bi-Sb-Te is mechanically soft followed by rapid compressing, such as by using a vertically rapidly descending forging hammer used in the steel mill).

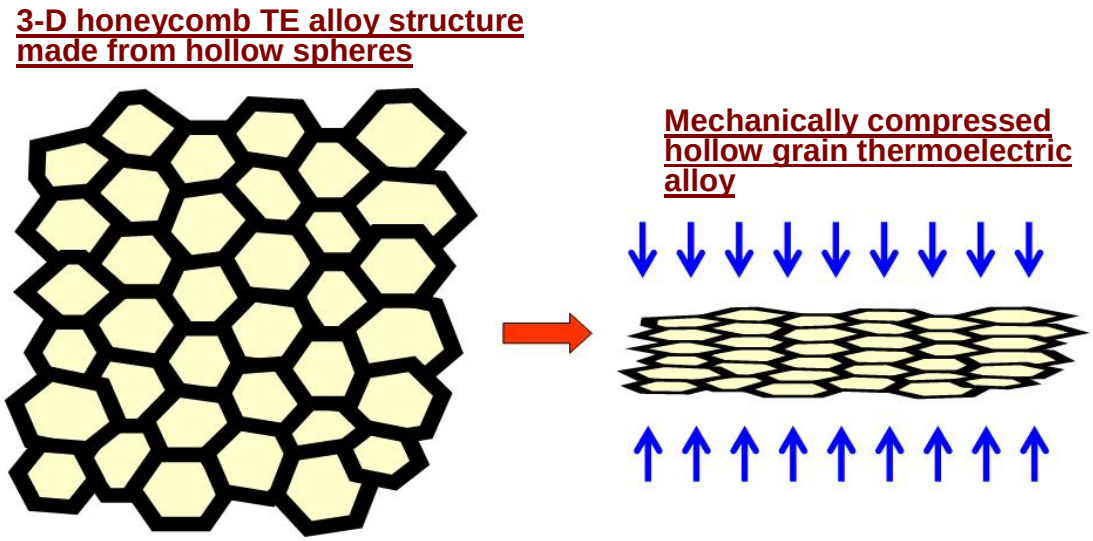

Figure 34. Schematic illustration of the mechanical compression forming of hollow honeycome thermoelectric alloy.

The nitrogen gas previously trapped within each Bi-Sb-Te hollow compartment can be allowed to escape as the hollow compartment is flattened and some local fracture occurs. An upper limit of plastic deformation is exhibited in the case of the completely flattened structure produced when the fragmented nanowall pieces are press formed (or cold welded) into consolidated metallic solid form.

A further advanced geometry that can be derived from the hollow sphere TE alloy is the incorporation of phonon-scattering foreign nanoparticles such as SiO_2 (having 4 nm diameter). This is illustrated in Figure 35. The fractured nanowall Bi-Sb-Te fragments are mixed with 0.1 – 2 % of SiO_2 nanoparticles (e.g., in colloidal solution),

Al_2O_3, or other nanoparticles. The mixture is then dried, compressed, and consolidated, using SPS or RPS sintering method.

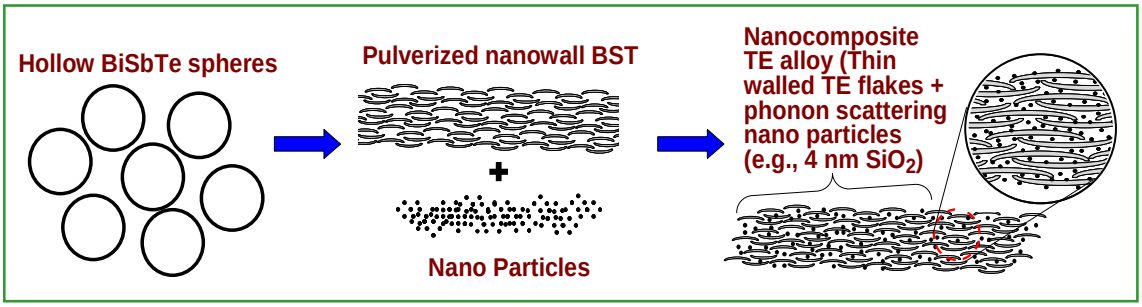

Figure 35. Schematic illustration of the fabrication of nanostructured thermoelectric alloy with 10 nm thickness flakes decorated with 4 nm phonon-scattering nanoparticles, followed by rapid sintering consolidation.

The hollow nanostructure of Figure 34 or 35 can be considered a light-weight thermoelectric alloy. Because the power output of the thermoelectric material depends on the amount of TE alloy involved, the thickness of this light-weight thermoelectric alloy has to be increased to yield the same amount of electricity, but since the 10 nm thickness nanostructure will reduce the thermal conductivity significantly (e.g., by a factor of 2), the overall TE efficiency (ZT value) will increase (e.g., by the same factor of 2).

The thermal conductivity and ZT behavior of the nanowall TE material were modeled and calculated by Professor Renkun Chen's Group. For the 10 nm thick nanowall sphere of Te alloy, the grain size is expected to be also in the regime of ~10 nm (assuming isotropic grain shape). Figure 36 illustrates the percentage of thermal conductivity contributed by the phonons versus the mean-free-path (MFP) smaller than the value. The results of phonon transport modeling of nanowall TE alloy for thermal conductivity and ZT properties at room temperature (T=300K), assuming that the

transport properties remain the same, are shown in Figure 37, and that for 373K is shown in Figure 38. As summarized in Table 2, the nanowall TE alloy can produce room temperature ZT ~1.3-1.4, which increases to ZT=1.6-1.7 at 373K. At room temperature, for 10 nm grain size, our calculated lattice thermal conductivity k_L = 0.47 W/m-K and ZT = 1.3~1.4. At 373 K (100°C), for 10 nm grain size, lattice thermal conductivity k_L = 0.32 W/m-K, and ZT = 1.6~1.7.

This modeling is based on a pure Bi-Sb-Te alloy. If phonon-scattering defects such as nanoparticles are also incorporated to the nanowall TE, substantially higher ZT can be expected.

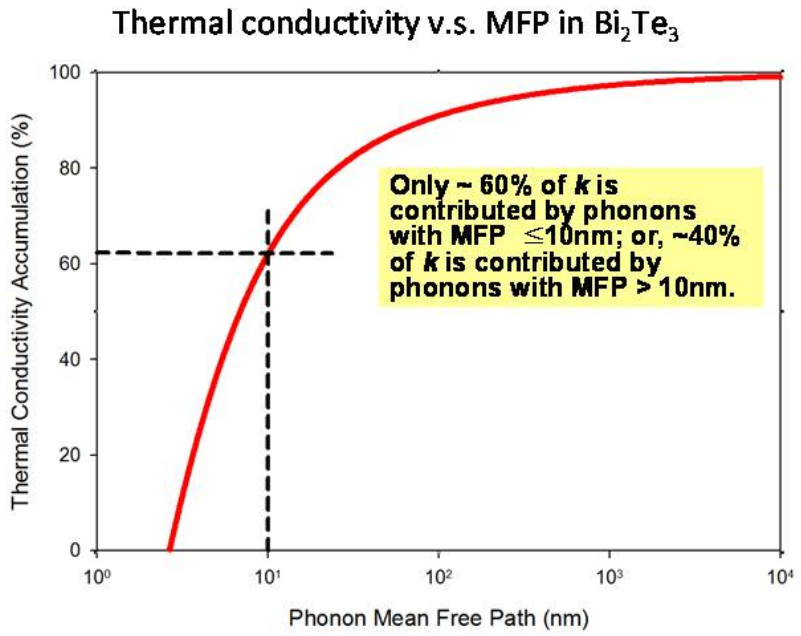

Figure 36. Illustration of the percentage of thermal conductivity contributed by the phonons with the mean-free-path (MFP): The graph shows the percentage of thermal conductivity contributed by the phonons with MFP smaller than the value in *x* axis.

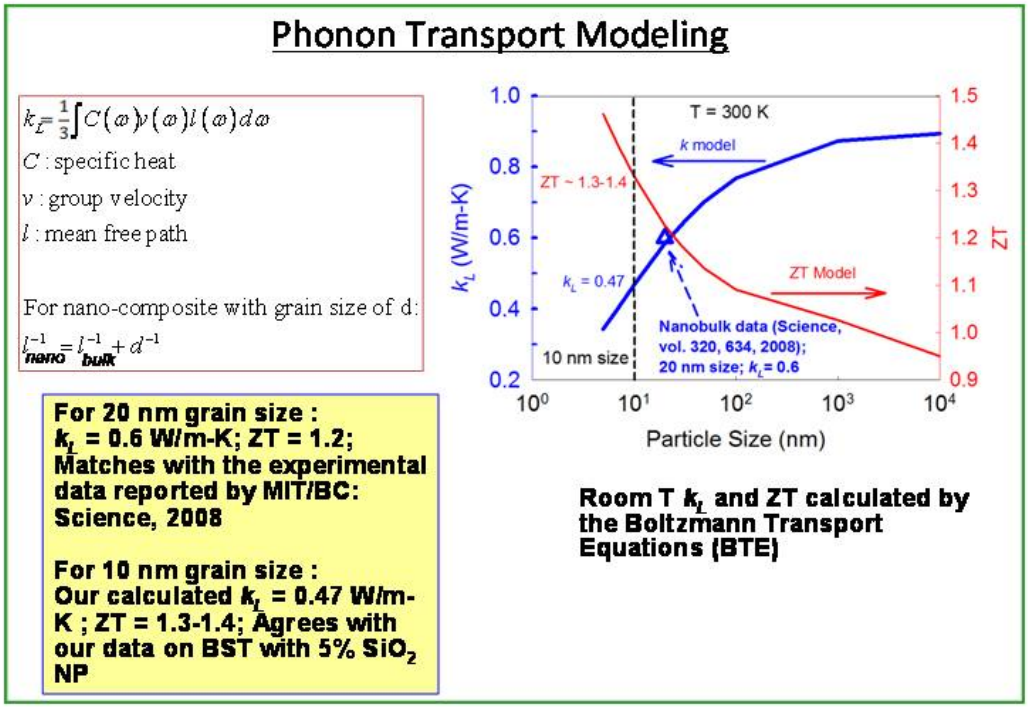

Figure 37. Phonon Transport Modeling of nanowall TE alloy for thermal conductivity and ZT properties at room temperature (T=300K).

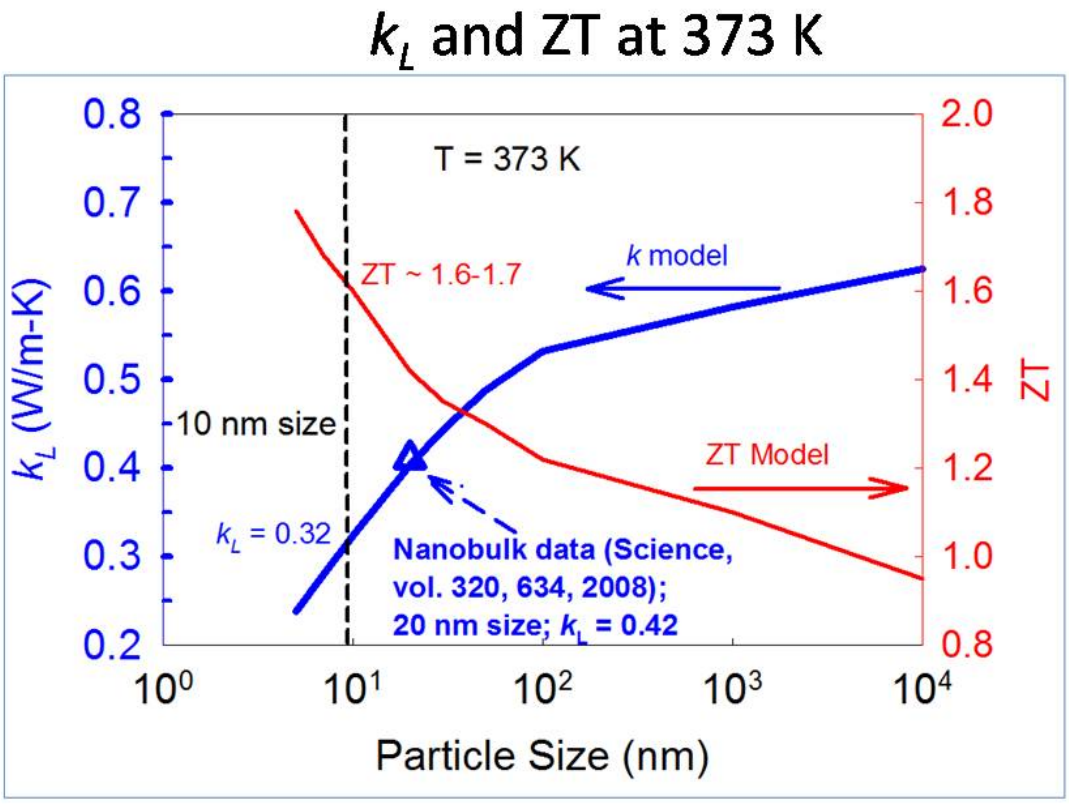

Figure 38. Phonon modeling of nanowall TE alloy at 373K for thermal conductivity and ZT properties.

Table 3. Estimated ZT values (modeling based) for various dimension of nanowall TE alloy.

Temp.	K_L at 10nm	ZT At 10nm	K_L at 20nm	ZT at 20nm	Bulk K_L	Bulk ZT
300K	0.47	1.3~1.4	0.6	1.2	0.91	~1
373K	0.32	1.6~1.7	0.43	1.4	0.8	~1

3.3 Spark Plasma Sintering (SPS) and Rapid Pulse Sintering (RPS) Results

3.3.1 Spark Plasma Sintering (SPS)

Spark Plasma Sintering (SPS) combines mechanical pressing and electrical heating techniques and is a method of producing densely sintered bodies using spark currents with minimal grain or microstructural coarsening. In SPS, pulsed DC current is passed through the graphite die as well as the powder compact in the case of an electrically conductive sample. Therefore, the heat is generated externally as well as internally in contrast to the conventional hot pressing where the heat is only provided by external heating. Therefore, a very high heating rate (up to 1000 K/min) is provided with the sintering process generally taking a few to several minutes. Whether or not plasma is generated has not been confirmed yet, especially for electrically insulating samples, but the enhanced densification effect is well known.

The method has received much attention in recent years as a sintering process of thermoelectric alloys due to the maintenance (or minimized coarsening) of phonon-scattering defects during sintering. The principle and machine structure is schematically illustrated in Figure 39. In traditional hot pressing of a powder compact, it is necessary to apply high temperatures to avoid pores inside the sample, and the associated time for sample heating and cooling resulted in undesirable grain growth. The Spark Plasma Sintering (SPS) is one of the techniques that can solve this problem.

In this research, we also utilized SPS for densification of either spark eroded or mechanically ground TE powders (with optional addition of phonon-scattering nano dispersoid particles such as 4 nm diameter SiO_2 nanoparticles or ~10 nm Ag

nanoparticles). Our samples were placed inside a graphite cylinder, vacuum pumped, and then compressed with a DC current on the powders and graphite cylinder.

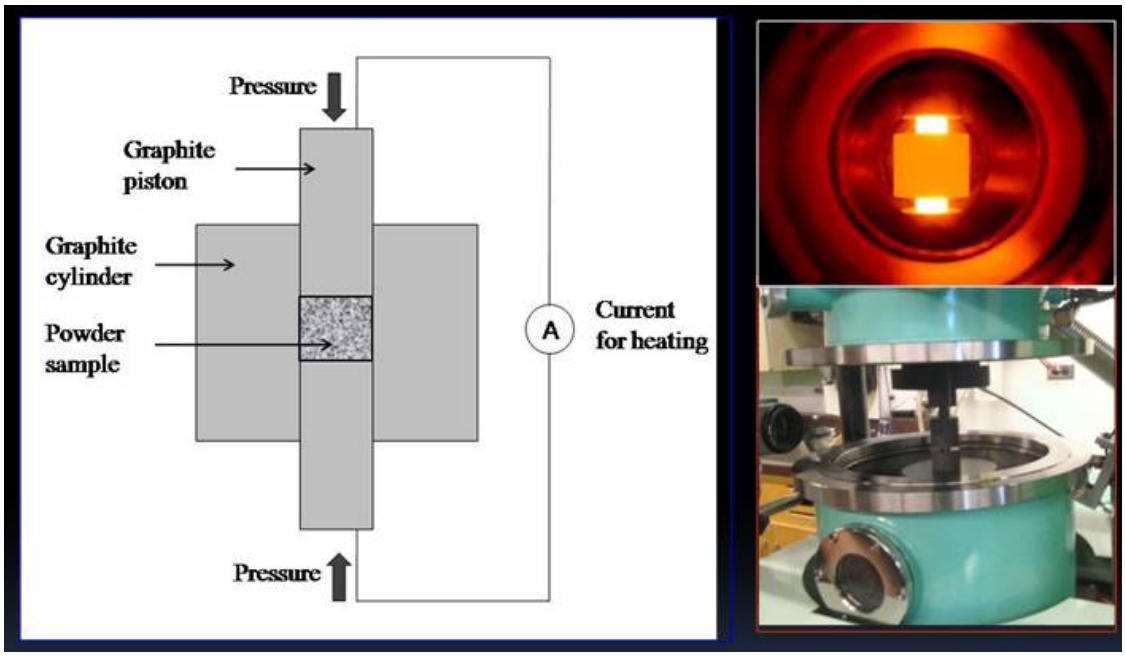

Figure 39. Schematic of Spark Plasma Sintering (SPS) utilized for TE alloy powder sintering.

The advantage of the SPS system is the rapid densification in a relatively short time compared to the hot pressing process. To maximize ZT value, the temperature, pressure and holding time are optimized. The Spark Plasma Sintering (SPS) system used was Dr. Sinter SPS model by Sumitomo Coal Mining in Japan. An electric current (2000 A) was passed through the graphite cylinder and powder sample in a vacuum chamber, and the optimized pressure of 50 MPa was applied on the powder sample. The temperature applied was between 400°C~500°C. The nanocomposite structure of $Bi_{0.5}Sb_{1.5}Te_{3.0}$ alloy was fabricated by grinding the alloy powder in a high-power attrition

mill to ~100 nm average particle size, mixing with 0.5-5 % (volume ratio) of 4 nm SiO_2 nanoparticles in colloidal solution, drying, and SPS sintering at various temperatures and time. Typical Seebeck coefficient values were S=230~245 μV/K, with this value for the Bi-Sb-Te sample containing SiO_2 nanoparticles being slightly higher than that for the bare Bi-Sb-Te sample.

The σ values for the Bi-Sb-Te samples containing 0.5~5 % (volume ratio) of 4 nm SiO_2 nanoparticles varied from ~40,000 to ~60,000 [S/m] depending on the SPS processing specifics. The power factor value of $S^2\sigma T$ [W/m-K] was obtained from the Seebeck Coefficient and electrical conductivity, with the power factor values ranging from 0.77~1.07 W/m-K depending on the SPS processing temperature and time.

The typical SPS sintering process utilized was 450~500°C for 5~10 minute sintering at 50 MPa pressure and vacuum with a heating rate of 100°C/min. The addition of SiO_2 to Bi-Sb-Te under similar SPS processing had a relatively small effect on the power factor values. The thermal conductivity of the 5% (volume ratio) SiO_2 nanoparticle containing Bi-Sb-Te sample was substantially reduced, with the lowest value being 0.69 W/m-K. The lattice thermal conductivity portion was k_L = 0.42 W/m-K and it is the lowest lattice thermal conductivity reported for Bi-Sb-Te. This experiment confirms that a Bi-Sb-Te sample containing nanoparticles is the right direction for controlling the thermal conductivity.

3.3.2 Rapid Pulse Sintering (RPS)

New, much more rapid sintering techniques and machinery have been developed in our laboratory to cope with the slow-cooling problem in the traditional SPS sintering. We named the technique the “Rapid Pulse Sintering (RPS)”. While the SPS has many advantages over a traditional hot pressing method, it still uses part of the heat generated from thr graphite cylinder surrounding the sample. This naturally poses the problem of slow cooling due to the extended time (at least minutes to tens of minutes) it takes to dissipate the thermal mass after the SPS sintering is done at high temperature. This slow cooling time is disadvantageous towards preventing grain growth or coarsening of nanostructured phonon-scattering centers intentionally introduced to the TE alloy samples.

The Rapid Pulse Sintering (RPS) system uses only heat induced from the resistivity of the powder sample for densification and does not use an external graphite die at all. Because it has an electrically insulated surrounding cylinder made of alumina, all of the current applied goes through “only” the powder compact sample between the upper and lower stainless steel punches so that resistive heat along the powder is maximized. The alumina cylindrical chamber also serves as a thermal insulator so that directional rapid cooling or rapid solidification takes place along the vertical direction. Figure 40 schematically shows the structure of the new Rapid Pulse Sintering (RPS) system. A high density of grain boundaries in thermoelectric alloys would increase phonon scattering with minimal electron scattering thereby increasing ZT. As the RPS method delivers controlled power pulses at a selected rate directly to the sample to be sintered, rapid sintering of nano-grained thermoelectric powders can be enabled, which

provides significant advantages over other, previously used sintering methods such as SPS. We measured the electrical and thermal conductivities and the Seebeck coefficient on several $(6mm)^3$ sintered cubes.

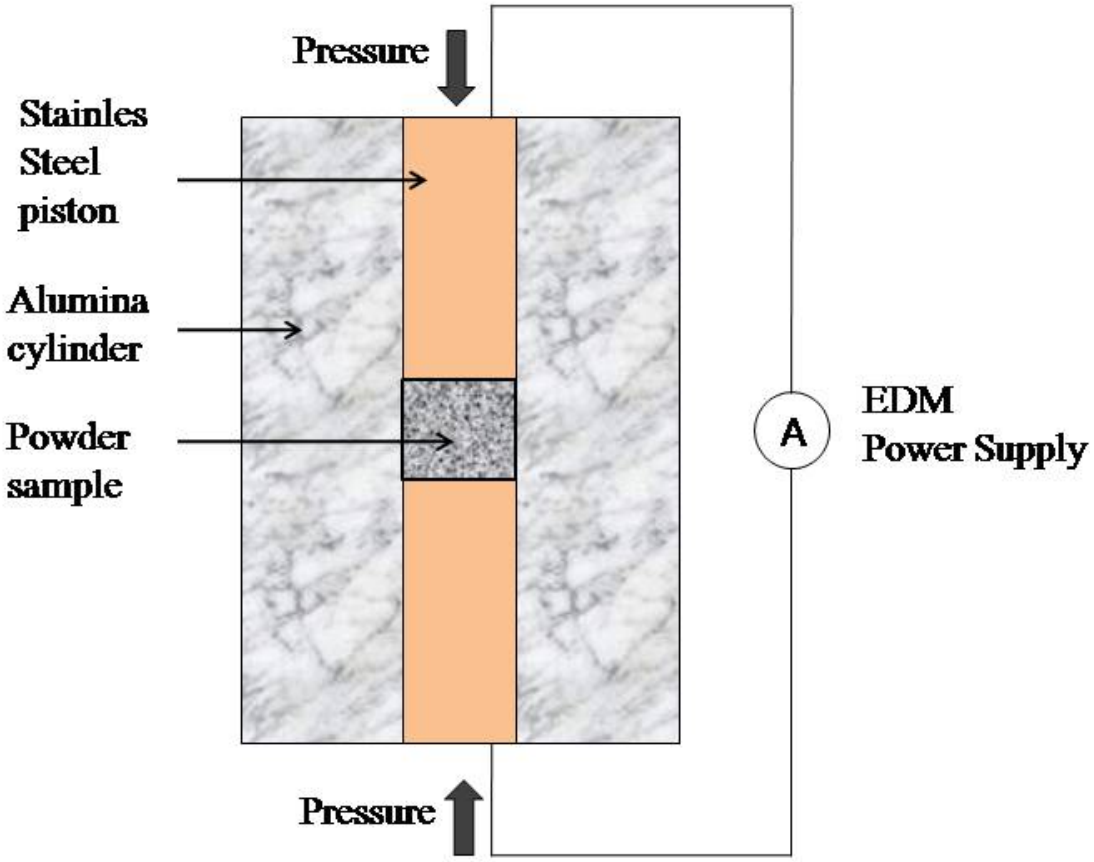

Figure 40. Schematic of Rapid Pulse Sintering (RPS) system.

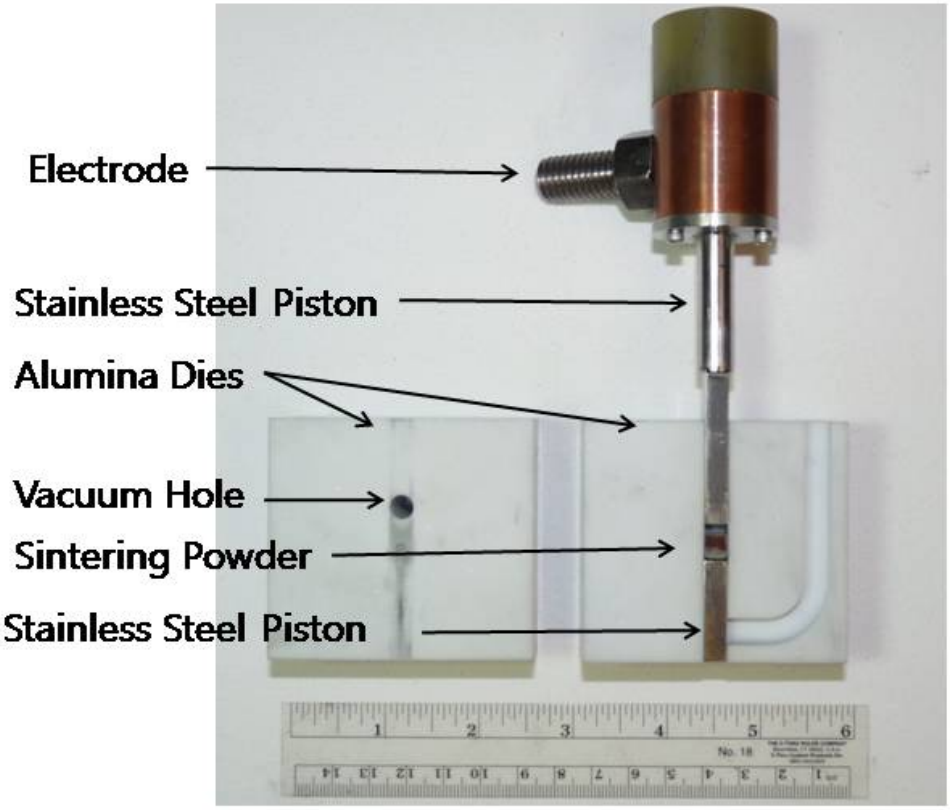

Figure 41. Picture of the Alumina (Al_2O_3) die and piston used in Rapid Pulse Sintering (RPS) system: The two halves of the Alumina (Al_2O_3) die with the sample between the top and bottom $6mm^2$ pistons placed in the $6mm^2$ channel of the die. In operation, the two die pieces are clamped together, and mounted in a vacuum tight chamber.

Power pulses are applied directly to the sample through the top and bottom pistons, with no current or heating in the insulating Alumina die. Power pulses are supplied by a Hansvedt EDM (Electric Discharge Machining) power supply, which permits complete control of the amplitude, width, and rate of the pulses.

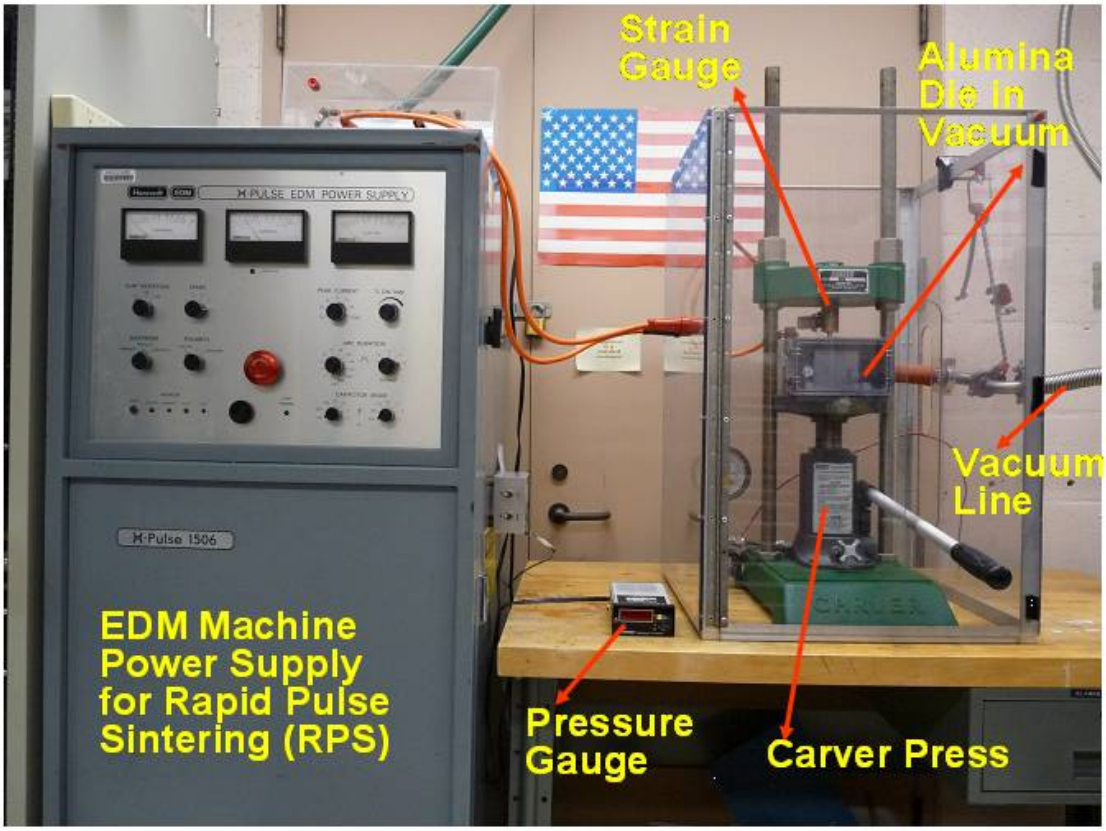

Figure 42. Rapid Pulse Sintering (RPS) System: EDM power supply, Carver presser and vacuum system.

Figure 42 shows the Rapid Pulse Sintering (RPS) system with the vacuum box containing the die and pistons mounted in a Carver press and connected to the EDM supply and a vacuum pumping system. Current pulses can be selected up to 600 Amp, with widths up to 120μ-sec (Figure 43), and duty cycles up to 50%, are applied directly to the $(6mm)^3$ samples in a 10^{-5} torr range vacuum while being pressed at the desired pressure.

The typical RPS sintering we employed takes only 3~60 seconds. This is an extremely fast sintering process, which gives practically no time for any grain or particle

coarsening during this sintering process. Assuming 10% duty cycle is equivalent to ~3 seconds total heating time, there are 3 sec/120 μsec = ~25,000 pulses of heating to ~600 amps. The temperature reached during RPS sintering is roughly estimated to be near or slightly above the melting temperature (~550°C) of the $Bi_{0.5}Sb_{1.5}Te_{3.0}$ alloy. A further advantage of the RPS is the rapid cooling provided by the pistons as the sintered samples are in direct physical contact above and below with metallic, high thermal conductivity pistons (copper alloy or stainless steel). This rapid cooling is a significant advantage in contrast to SPS sintering in which the cooling of graphite and associated surrounding mechanical structures take an order of magnitude greater amount of time.

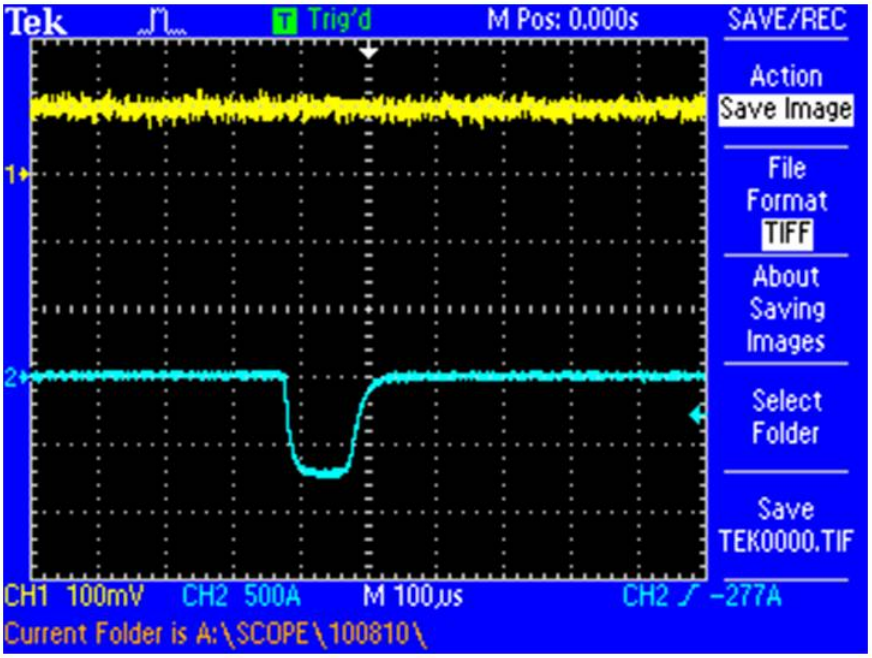

Figure 43. EDM pulse signal of 600 amp and 120μ-sec used for Rapid Pulse Sintering (RPS) System.

These conditions are adequate to produce near bulk densities from nano-powders in < 30 seconds. We have measured (Table 3) the density of RPS sintered Bi-Sb-Te powder compact to be as high as d~6.42 g/cm^3 (corresponding to ~95% density) as compared to the full density of Bi-Sb-Te bulk material (d~ 6.74 g/cm^3). The flexibility in specifying the power conditions, the modest structural and power requirements, and the fast sintering speed provide clear advantages over systems such as Spark Plasma Sintering.

Table 4. Density of RPS processed Bi-Sb-Te samples

Material	Applied Force (lb)	Holding Time (s)	Duty Cycle (%)	Density (%)
$Bi_{0.5}Sb_{1.5}Te_{3.0}$	2000	30	4	94.3
$Bi_{0.5}Sb_{1.5}Te_{3.0}$	2000	30	4	95.3
$Bi_{0.5}Sb_{1.5}Te_{3.0}$	1000	3	40	95.6

Figure 44 shows surface SEM images before (left figure) and after (right figure) Rapid Pulse Sintering (RPS) process. It shows RPS system is very effective tool in sintering TE powders to a high-density solid structure.

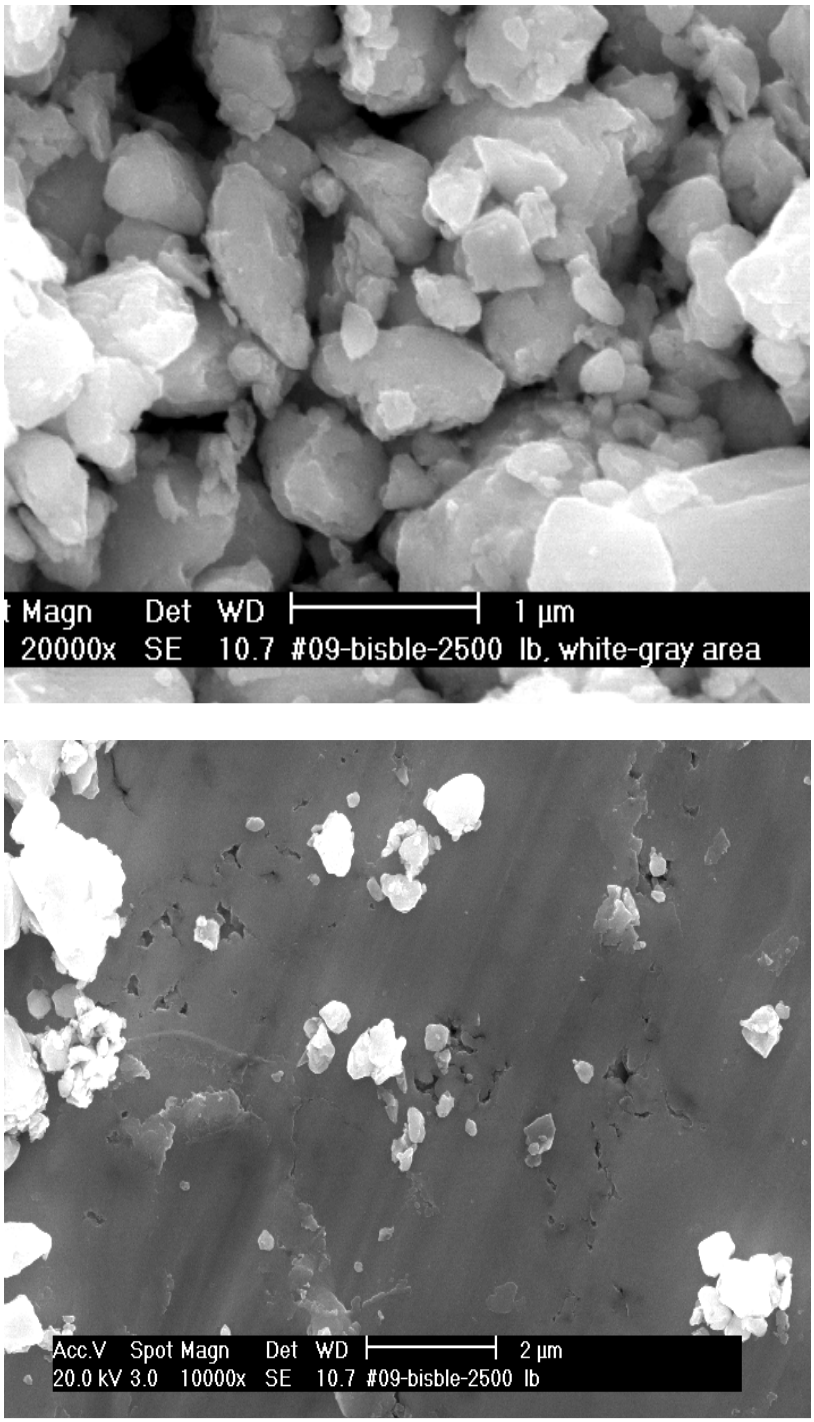

Figure 44. Surface SEM images before (top) and after (bottom) Rapid Pulse Sintering (RPS) process.

Table 4 shows the electrical property comparison between Spark Plasma Sintering (SPS) and Rapid Pulse Sintering (RPS) processes with identical composition powders. It indicates that RPS process with only a 60 second holding time produces almost equivalent electrical performance compared to SPS processed samples which have 5 to 10 times longer holding times.

Table 5. Electrical property comparison between SPS vs RPS

Sintering Method	Material	Holding Time (s)	Electric Conductivity (1/ohm-m)	Seebeck (μV/K)	Power Factor
SPS	$Bi_{0.5}Sb_{1.5}Te_{3.0}$	300	4.8E+04	230.6	0.766
SPS	$Bi_{0.5}Sb_{1.5}Te_{3.0}$	600	4.9E+04	230.1	0.788
RPS	$Bi_{0.5}Sb_{1.5}Te_{3.0}$	60	4.5E+04	238.2	0.773

CHAPTER 4. Conclusions and future directions

4.1 Conclusions

In this thesis, innovative and cost effective approaches for the fabrication of nanostructured bulk materials for thermoelectrics are described and discussed. It is expected that these new techniques will contribute to developing many novel thermoelectric materials and other innovative and useful materials.

Successful fabrication of spark eroded nano-grained Bi-Sb-Te thermoelectric compounds, copper-jacketed deformation, successful compaction and nano-defect engineering is presented. A practical methodology of measuring bulk thermal conductivity from ribbon-dimensioned thermoelectric material geometry using 3ω technique has also been established. As a result, substantial progress has been made in improving the thermoelectric material properties through reduction in thermal conductivity and enhanced ZT figure of merit (ZT~1.4 at room temperature).

Spark erosion method is also presented as a very effective tool to produce thermoelectric nanocomposite particles. Bi-Sb-Te particles embedded with the nano-particles of SiO_2 are fabricated by spark erosion method, which may be utilized for creating a new TE alloy structure consisting of Bi-Sb-Te matrix with uniformly dispersed phonon-scattering nanoparticles. In addition, spark erosion technique in liquid nitrogen dielectric leads to a discovery of new, nanowall hollow Bi-Sb-Te thermoelectric alloys with the wall thickness as small as ~10 nm. Such a nanoscale dimension offers a potential to manipulate the nanostructure and achieve light-weight, high ZT nanocomposites. Modeling and calculation of thermal conductivity and ZT for the nanowall Bi-Sb-Te alloy using the Boltzmann Transport Equations (BTE) predict that the ZT values can

reach 1.6~1.7 for the pure Bi-Sb-Te alloy. With an addition of phonon-scattering defects, the ZT values could be increased to substantially higher values.

New, Rapid Pulse Sintering (RPS) processing technique has been developed and the machinery has demonstrated the rapid consolidation of thermoelectric materials. The Rapid Pulse Sintering (RPS) can be completed typically in as fast as 3 to 60 seconds. The cooling speed is also extremely fast (much faster than SPS process) since the top and bottom pistons are both made of high thermal conductivity metal. This technique can be used for the synthesis of various new TE alloys as phonon-scattering defects can be retained during the alloy consolidation process. Rapid solidification of various molten TE alloys can also be achieved. Additional optimizations of process and material parameters could lead to much higher ZT value for promising advances toward a wide range of commercial applications of the Bi-Sb-Te thermoelectric alloy.

4.2 Future directions

Beyond the research introduced in this thesis, the following future works will be very worthy of enhancing the performance of thermoelectric materials.

The phonon transport modeling of nanowall TE alloy for thermal conductivity and ZT properties is an interesting result that needs to be verified through experiments. For this purpose, spark erosion process for hollow nano-walled particles should be extensively studied to control the thickness and grain size of the nano-wall of the particles.

The RPS (Rapid Pulse Sintering) process is also the great area for further research. The detailed mechanisms of how the rapid sintering could be possible need

more research with precise control of the parameters including pressure, temperature, electric power, and holding time.

Lastly, the nanocomposite particles produced by the spark erosion process are the materials of interest, and experiments are needed to test its thermoelectric properties. For this purpose, we need further study of how to control the amount of nanoparticles processed into the spark eroded TE particles.

In conclusion, all of these new approaches will be great journeys of the search for innovative TE materials for the researchers who will challenge these exciting areas.

REFERENCES

1. "*Thermoelectrics Handbook"*, ed. D.M. Rowe, CRC Press, Boca Raton, FL, (2006)

2. M. S. Dresselhaus, J. P. Heremans, in "*Thermoelectrics Handbook:Macro to Nano"* (Ed: D. M. Rowe), Taylor and Francis, CRC, Boca Raton, FL, Ch. 39, p. 39-1–39-24 (2006).

3. Hicks, L. D. and M. D. Drsselhaus, "Thermoelectric figure of merit of a one-dimensional conductor", Physical Review B47, 16631 (1993).

4. Dresselhaus, M. D.; Lin, Y. M.; Black, M. R.; Rabin, O.; Dresselhaus, G. In *"New directions for Low Dimensional Thermoelectricity"*, Materials Reserach Society Symposium, Boston, MA, 2003; Nolas, G. S.; Yang, J.; Hogan, T. P.; Johnson, D. C., Eds. Materials Research Society: Boston, MA, 2003.

5. R. Venkatasubramanian, E. Siivola, T. Colpitts, B. O'Quinn, *"Thin-film thermoelectric devices with high room-temperature figures of merit"*, Nature 413, 597 (2001).

6. T. C. Harman, P. J. Taylor, M. P. Walsh, B. E. LaForge,*"Quantum dot supperlattice thermoelectric materials and devices"*, Science 297, 2229 (2002).

7. K. F. Hsu, S. Loo, F. Guo, W. Chen, J. S. Dyck, C. Uher, T. Hogan, E. K. Polychroniadis, M. G. Kanatzidis, Science 303, 818 (2004).

8. J. P. Fluerial, T. Caillat, A. Borshchevsky, in *Proceedings of the 13th International Conference on Thermoelectrics*, Kansas City, MO, 30 August to 1 September 1994 (AIP, New York, 1995), pp. 40–44.

9. M. S. Dresselhaus , G. Chen, M. Y. Tang, R. G. Yang, H. Lee, D. Z. Wang, Z. F. Ren, J.-P. Fleurial, P. Gogna, *"New Directions for Low-Dimensional Thermoelectric Materials"*, Adv. Mater. 19, 1043 (2007).

10. X. B. Zhao, X. H. Ji, Y. H. Zhang, T. J. Zhu, J. P. Tu, and X. B. Zhang, *"Bismuth telluride nanotubes and the effects on the thermoelectric properties of nanotube-containing nanocomposites"*, Appl. Phys. Lett. 86, 062111 (2005).

11. Akram I. Boukai, Yuri Bunimovich, Jamil Tahir-Kheli, Jen-Kan Yu, William A. Goddard III, and James R. Heath, *"Silicon nanowires as efficient thermoelectric materials"*, Nature 451(10), 168 (2008)

12. Deyu Li, Yiying Wu, Philip Kim, Li Shi, Peidong Yang, Arun Majumdar, *"Thermal conductivity of individual silicon nanowires"*, Appl. Phys. Lett. 83, 2934 (2003).

13. A. I. Hochbaum, R. Chen, R. D. Delgado, W. Liang, E. C. Garnett, M. Najarian, A. Majumdar, and P. Yang, *"Enhanced Thermoelectric Performance of Rough Silicon Nanowires"*, Nature 451(10), 163 (2008).

14. K. Q. Chen, W. X. Li, W. Duan, Z. Shuai, and B. L. Gu, *"Effect of defects on the thermal conductivity in a nanowire"*, Phys. Rev. B 72, 045422 (2005).

15. B. Poudel, Q. Hao, Y. Ma, Y. Lan, A. Minnich, B. Yu, X. Yan, D. Wang, A. Muto, D. Vashaee, X. Chen, J. Liu, M. S. Dresselhaus, G. Chen, and Z. Ren, *"High-Thermoelectric Performance of Nanostructured Bismuth Antimony Telluride Bulk Alloys"*, Science 320, 634 (2008).

16. Venkatasubramanian, E. Siivola, T. Colpitts and B. O'Quinn, *"Thin-film thermoelectric devices with high room-temperature figures of merit"*, Nature 597 (2001).

17. Disalvo, F. J., *"Thermoelectric Cooling and Power Generation"*, Science, 285, 703–706 (1999).

18. Tritt, T. M., Ed.; Academic Press: San Diego, Vol. 69, pp 51-100 (2000).

19. Sales, B. C., *" Thermoelectric materials - Smaller is cooler"*, Science, 295(5558), 1248–1249 (2002).

20. Snyder, G. J., *"Complex thermoelectric materials"*, Toberer, E. S. Nat. Mater., 7(2), 105–114 (2008).

21. Nolas, G. S.; Poon, J.; Kanatzidis, *"Recent developments in bulk thermoelectric materials"*, M. Mater. Res. Soc. Bull., 31(3), 199–205 (2006).

22. Chung,D. Y.; Iordanidis, L.; Choi, K. S.; Kanatzidis, M. G. Bull. Kor. Chem. Soc., 19(12), 1283–1293 (1998).

23. Mrotzek, A.; Kanatzidis, " Design in Solid State Synthesis", M. G. Acc. Chem. Res., 36(2), 111–119 (2003).

24. Sootsman, J. R.; Chung, D. Y.; Kanatzidis, M. G., *"New and Old Concepts in Thermoelectric Materials"*, Angew. Chem., Int.Ed. (2009).

25. Medlin, D. L.; Snyder, G. J., *" Interfaces in bulk thermoelectric materials"*, Curr. Opin. Colloid Interface Sci., 14(4), 226–235 (2009).

26. A.J. Minnich, M.S. Dresselhaus, Z.F. Ren and G. Chen, *"Bulk nanostructured thermoelectric materials: Current research and future prospects"*, Energy Environ. Sci., 2, 466-479 (2009).

27. Terry M. Tritt, Harald Böttner, and Lidong Chen, *"Thermoelectrics: Direct Solar Thermal Energy Conversion"*, MRS Bulletin, vol. 33, p.366 (2008).

28. A.E. Berkowitz and J.L. Walter, *"Spark erosion: A method for producing rapidly quenched fine powders"*, J. Mater. Res. 2(20), 277-288, Mar/Apr (1987)